On the Influence of Latent and Sensible Heating for Maintaining Baroclinicity in the Gulf Stream Region

Master's Thesis in Meteorology

Ståle Dahl-Eriksen

June 2016

UNIVERSITY OF BERGEN
GEOPHYSICAL INSTITUTE

Abstract

For the North Atlantic storm track to collocate with the ocean front, there has to be efficient restoring mechanisms for baroclinicity. The total diabatic heating is agreed to play the most dominant role, but whether the differential surface sensible heat fluxes or the latent heat release have the strongest impact, is still an ongoing discussion.

This study presents a synoptic comparison between intense surface sensible heat fluxes and latent heating in the Gulf Stream region. During two winter seasons, 2008-2010, the findings show that intense latent heat release is strongly connected to the warm sector of extratropical cyclones. This study also shows that intense surface sensible heat fluxes are highly influenced by a persistent anticyclonic pattern over the North American continent prior to their peak. The latter indicates that anticyclones also contribute to strong surface sensible heat fluxes and possibly help to maintain baroclinicity in the Gulf Stream region.

When using the slope of an isentropic surface as a proxy for baroclinicity, it is found that an increase in the surface sensible heat fluxes is followed by a low tropospheric steepening of the net isentropic slope. The latent heat release does not influence the net isentropic slope in the same distinct way, but when investigating its tendency to increase the slope, the latent heat release shows positive contributions above 900 hPa. The overall findings indicate that both surface sensible heat fluxes and latent heating restore baroclinicity in the Gulf Stream region, with the former showing strongest indications.

Acknowledgements

I would like to thank my two supervisors, Thomas Spengler and Lukas Papritz, for all the support and encouragement during the last year. I have very much appreciated your enthusiasm regarding my project and you have both made my "research career" very interesting. A special thanks to Lukas for providing me with his slope tendency diagnostics and for helping me with both meteorological and technical problems throughout this whole year. I must also acknowledge the whole "Dynmet Family" for many funny discussions, as well as a great trip to Norwich.

I want to express my sincere gratitude to my always supporting family. All comforting words and financial help during the last five years have made my time as a student much easier. An extraordinary thanks to my one and only brother, Vegard, for proofreading my thesis when I needed it the most. Your help was exceptional.

I have to thank and apologize to my remarkable girlfriend, Tina, for being non-existent the last couple of months. Your patience has made it easier to get through these busy times.

And finally, thanks to my fellow students at GFI. I could not have asked for a better mix of personalities. I have had so much fun during the last five years. I will never forget all the hilarious moments and crazy evenings. I am always reachable on my waffle phone. Thank you all.

Contents

List of Abreviations

NA	**N**orth **A**tlantic
US	**U**nited **S**tates
SST	**S**ea **S**urface **T**emperature
LH	**L**atent **H**eat
EC	**E**xtratropical **C**yclone
WCB	**W**arm **C**onveyor **B**elt
SSHF	**S**urface **S**ensible **H**eat **F**luxes
CAO	**C**old **A**ir **O**utbreak
CAM	**C**old **A**ir **M**ass
PV	**P**otential **V**orticity
LHS	**L**eft **H**and **S**ide
RHS	**R**ight **H**and **S**ide
YOTC	**Y**ear **O**f **T**ropical **C**onvection
IFS	**I**ntegrated **F**orecasting **S**ystem
DJF	**D**ecember **J**anuary **F**ebruary

Chapter 1

Background

1.1 Introduction

Mid-latitude storms are frequently observed in confined regions known as storm tracks (Small et al., 2014). In the North Atlantic (NA), such a storm track begins at the east coast of the United States (US) and follows a north-eastwards direction towards Europe (Brayshaw et al., 2011). Studies on the NA storm track date back to at least the 19th century. For instance, Hinman (1888) produced a chart over the NA (Fig. 1.1) as early as 1888, trying to illustrate regions with high storm frequency (dashed lines). Even though the chart is old, it still realistically represents the NA storm track (Chang et al., 2002).

The location of the NA storm track links with the position of the subtropical jet stream and the associated strong horizontal temperature gradient (Hartmann, 1994). Regions with strong horizontal temperature gradients are also called baroclinic zones (Holton and Hakim, 2012). One distinct baroclinic zone in the NA is the observed strong sea surface temperature (SST) gradient in Fig. 1.2. The SST-gradient is associated with a western boundary current known as the Gulf Stream. The Gulf Stream carries vast amount of warm waters along the east coast of the United States (US) and toward colder regions. It eventually leaves the continent and takes a more zonal path, hence contributing to the strong SST-gradient (Talley et al., 2011).

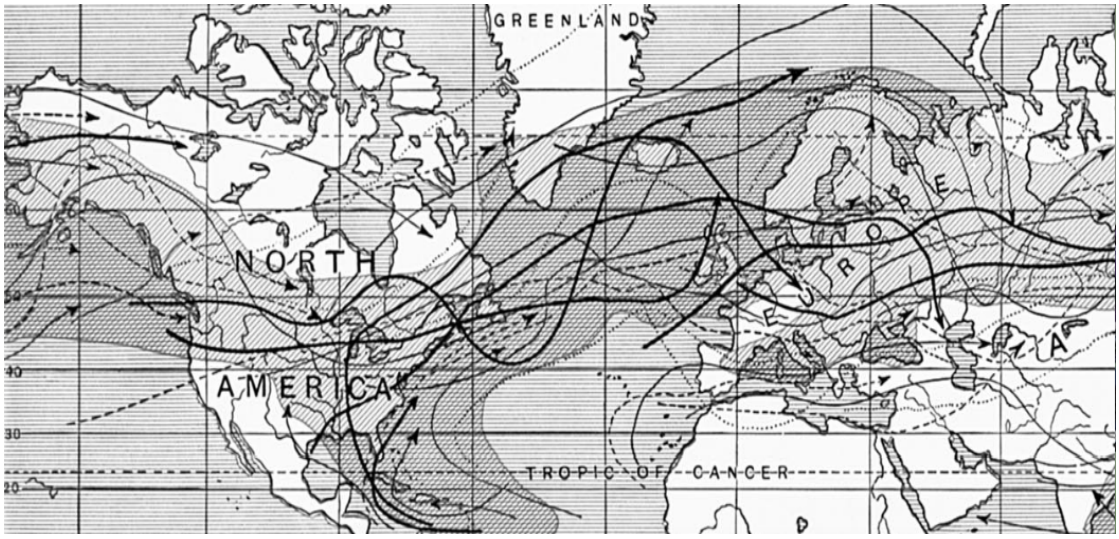

Figure 1.1: Storm frequency chart of the NA-region, originally produced by Hinman (1888), and adapted from Chang et al. (2002). Solid lines show individual storms and dashed lines show regions with high storm frequency.

A considerable amount of studies have pointed out the sensitivity between the NA storm track and the SST-gradient in the Gulf Stream (e.g., Palmer and Zhaobo, 1985; Hoskins and Valdes, 1990; Brayshaw et al., 2008; Woollings et al., 2010). For instance, Brayshaw et al. (2008) weakened and enhanced the SST-gradient through a series of idealized experiments and observed an increase in storm activity with a stronger SST-gradient. Woollings et al. (2010) investigated the NA storm track response to the SST-gradient for different model resolutions. When they imposed a higher model resolution, the SST-gradient got better represented and the storm track got aligned with the ocean front. The findings of Brayshaw et al. (2008) and Woollings et al. (2010) are also supported by Small et al. (2014) who smoothed the SST-gradient in a high resolution model and experienced the storm track to be less intense and also shifted away from the ocean front.

For the NA storm track to exist, it requires confined regions with persistently strong baroclinicity (Papritz and Spengler, 2015). However, growth of mid-latitude storms are actually known to reduce the baroclinicity (Chang and Orlanski, 1993). A weakening of the baroclinicity in a region, also makes the region less susceptible

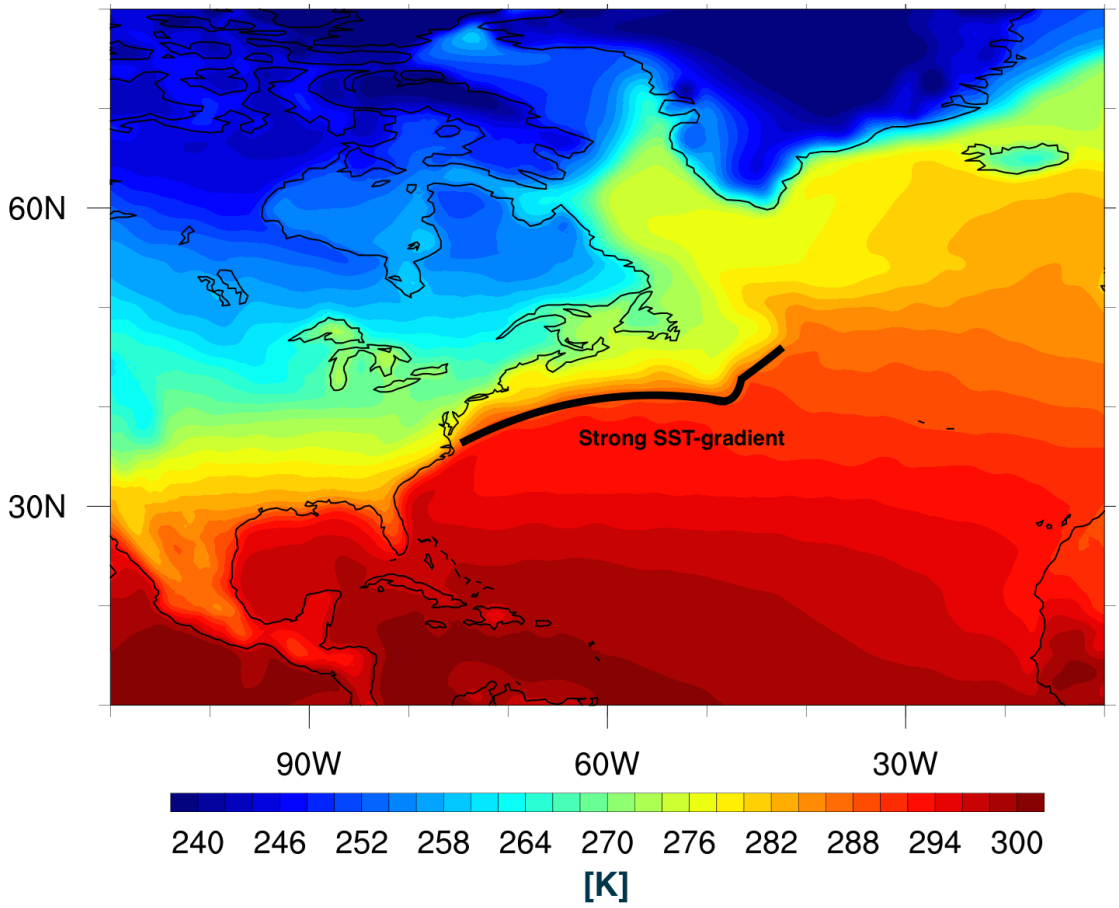

Figure 1.2: Time averaged surface temperatures (K) in the North Atlantic for DJF 2008-2010.

for consecutive storm formations. For storms to repeatedly collocate with the SST-front, baroclinicity must somehow be restored. Nakamura et al. (2004) explain the differential energy input from the Sun to restore some baroclinicity, but also argue that the solar radiation alone cannot provide a clear explanation for the existence of storm tracks. Nakamura et al. (2004) instead argue sensible heating, related to differential heat fluxes across the SST-gradient, to be most important. This has also been supported by Sampe et al. (2010) and Hotta and Nakamura (2011). However, Papritz and Spengler (2015) propose the most dominant restoring baroclinic process as the latent heat (LH) release associated with cloud formations over the warm ocean in the Gulf Stream.

Because we do not fully understand why the NA storm track aligns along the SST-front, this study will investigate the influence of latent and sensible heating for maintaining baroclinicity in the Gulf Stream region. Because the NA storm track affects populated areas, better understanding of how it interacts with the SST-gradient may advance the forecasts, potentially prevent extensive damages on infrastructure and save human lives.

1.2 Extratropical Cyclones

Following Holton and Hakim (2012), a mid-latitude storm is also known as an extratropical cyclone (EC). ECs exist because of the horizontal temperature differences in the atmosphere. They use the available potential energy associated with the horizontal temperature gradients and turns it into kinetic energy. This is known as growth by baroclinic instability. As ECs grow, more potential energy is converted into kinetic energy, which therefore reduces the temperature gradient.

ECs rotate counter clockwise in the Northern Hemisphere (NH) and clockwise in the Southern Hemisphere (SH). The reason for the rotation is owed to the fact that the Earth itself rotates. The Earth's rotation creates a force called the Coriolis force. Because a flow normally moves from high to low pressure, air around an EC gets sucked in towards its center (lowest pressure). On its way to the center, the Coriolis force deflects the air to the right (left) in NH (SH). We therefore say ECs rotate counter clockwise (clockwise). Holton and Hakim (2012) define a typical length scale of an EC to be around 1000 km in the horizontal. Length scales at this size are defined as synoptic length scales. ECs are therefore synoptic weather systems.

ECs form in regions with warm tropical air south of their low pressure center and cold polar air north of it. A counter clockwise rotation will therefore provide polewards warm air advection on the eastern side of an EC and equatorwards cold air advection on the western side (Fig. 1.3). For this reason, ECs are associated with frontal zones. Fronts are identified as a distinction between two air mass boundaries (Markowski and Richardson, 2010).

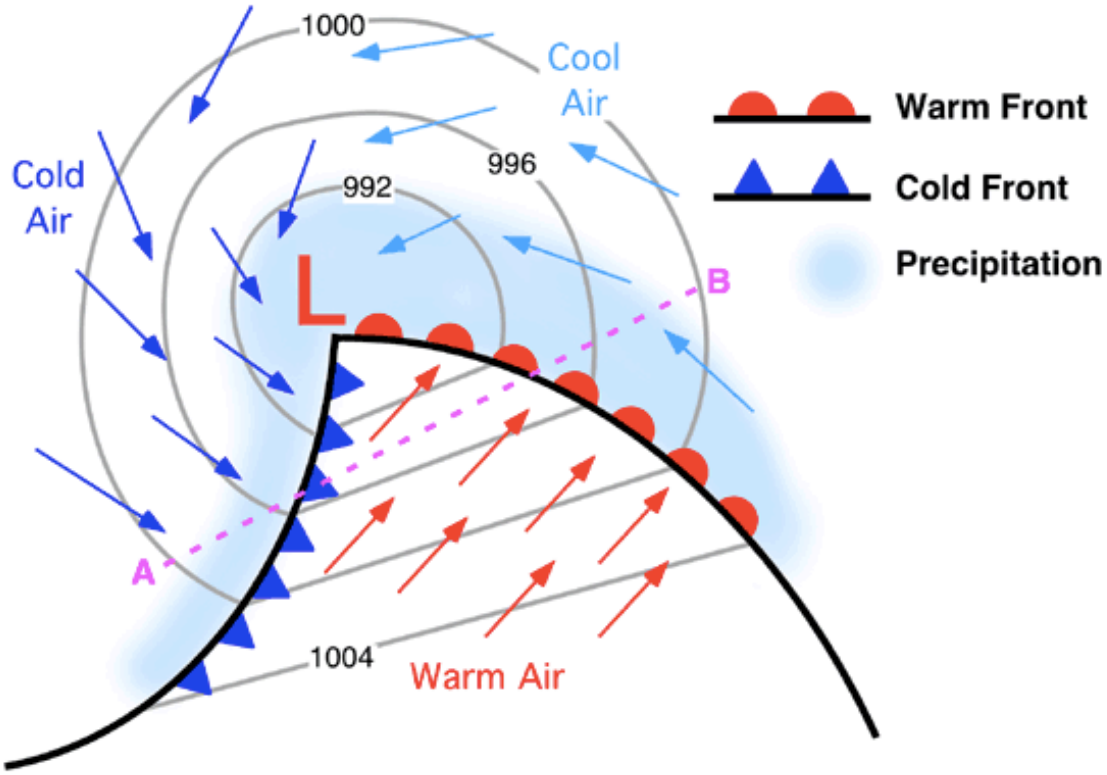

Figure 1.3: Figure adapted from Pidwirny (2006), showing the typical frontal structure in an EC. Grey lines are pressure contours (hPa), decreasing towards the lowest pressure (red L). The arrows show the movement of the wind, with colors representing the temperature.

We can see the typical frontal structure of an EC in Fig. 1.3. The warm air on the south-eastern side of the EC moves towards a colder region. The leading edge of the warm air marks what we call a warm front. On the north-western side of the EC, cold air moves into a region of warmer air. The leading edge of the cold air is therefore characterized as a cold front. The warm air behind the warm front and the cold air behind the cold front is sometimes called the warm and cold sector of an EC (Markowski and Richardson, 2010) (Fig. 1.3). The air-stream in the warm sector is associated with strong ascent and is known as the warm conveyor belt (WCB) (e.g., Madonna et al., 2014). The air stream in the cold sector is associated

with cold descending air (Vannière et al., 2016).

1.3 Latent Heating

Following Wallace and Hobbs (2006), cloud formations in the atmosphere typically occur when H_2O changes phase from gas (water vapour) to liquid (water). This process is known as condensation of water vapour. During condensation, heat is released to the environment, known as LH-release.

In an EC, much of the LH-release is related to the warm sector and thus the WCB (Madonna et al., 2014). Since the air in the WCB is warm, it can hold more moisture (water vapour) than the colder air. With more moisture comes also the ability to release more LH (Wallace and Hobbs, 2006). Madonna et al. (2014) points out that the WCB is responsible for transporting the largest amount of moisture from the boundary layer and into the free atmosphere. In addition, Pfahl et al. (2014) found that the WCB accounts for 70 % of all precipitation over the Gulf Stream region.

The strong precipitation and cloud formations in the Gulf Stream is also found by Minobe et al. (2008), who detected a deep convective layer along the SST-front with strong LH-release throughout the whole troposphere. Moreover, Papritz and Spengler (2015) investigated the LH-release in the NA and found maximum values on the warm side of the SST-front. Papritz and Spengler (2015) proposed the LH-release in their findings to play the most dominant role for maintaining baroclinicity along the Gulf Stream region, and therefore also keep this region conducive for consecutive storm formations.

What suggested by Papritz and Spengler (2015) is in agreement with Hoskins and Valdes (1990) who proposed the LH-release in individual ECs as the most important restoring baroclinic process along the NA storm track. Hoskins and Valdes (1990) suggested that ECs can feed on their self-induced LH-release. Because ECs propagate with a north-eastwards component in the NA, and much of the LH-release is triggered downstream of their low pressure (warm sector), the ECs can potentially harvest the self-induced baroclinicity as they propagate. Hoskins and

Valdes (1990) also argue the high winds associated with ECs to more strongly drive the Gulf Stream and to maintain the strong SST-gradients.

Different case studies have recently supported the idea of Hoskins and Valdes (1990), and shown that the intensity of individual ECs depends on their own LH-release. For instance, Ludwig et al. (2014) argued the intensification of the EC "Xynthia" to be highly dependent on LH-release. Xynthia originated over the south-western NA, in a region with anomalously high SST. Ludwig et al. (2014) argued the high SST to play a role for bringing more moisture to the atmosphere, creating a larger potential to release LH. The strength of Xynthia was substantially reduced in the model simulations when the surface moisture fluxes were turned off. Ludwig et al. (2014) explained the reduced ability to release LH as the dominant role for the weaker storm intensity, compared to the observations. Also Booth et al. (2012) investigated the response between LH-release and storm intensification. They did experiments of two independent winter storms that originated along the NA SST-front. Booth et al. (2012) observed a reduction in storm intensity when the storms were supplied with less moisture from the sea surface.

As we see, many studies agree that LH-release play a role for both intensifying storms and maintaining a storm track. Due to the extensive cloud formations and strong LH-release around the SST-front, LH-release is suggested to play an important role for anchoring the storm track along the Gulf Stream region. That being said, the idea of LH-release to maintain storm tracks has been questioned, because the LH-release mainly is confined to the free troposphere and cannot necessarily explain the maintenance of baroclinicity close to the surface (e.g., Nakamura et al., 2004; Hotta and Nakamura, 2011).

1.4 Sensible Heating

Following Marshall and Plumb (2007), the heat exchange between two substances of different temperatures, which not involves a phase change, is known as sensible heating. Upward directed surface sensible heating happens when a warm surface provides heat to a colder overlying substance. During winter in the mid-latitudes,

the ocean is often much warmer than the overlying air. It therefore exists a sharp air-sea temperature difference which generates strong upward directed surface sensible heating.

Differential surface sensible heat fluxes (SSHF) have been argued as the main process restoring low level baroclinicity along the SST-front. To understand the concept, let us visualize an EC travelling along the SST-front in the NA (see SST-front in Fig. 1.2). The cold sector of the EC advects cold air across the SST-front, which makes the air-sea temperature difference on the cold side of the SST-front significantly smaller than the air-sea temperature difference on the warm side. On the warm side, stronger SSHF are thus produced. This leads to differential SSHF across the SST-front. The differential SSHF warms the overlying air differently across the SST-front, increasing the baroclinicity in the lower troposphere.

Hotta and Nakamura (2011) argued the differential SSHF as the main reason for why baroclinicity is restored in the lower levels along the SST-front. They found that the effects from sensible heating to restore the low level baroclinicity were much stronger than the effects from LH. The findings of Hotta and Nakamura (2011) indicated the LH-release to only play a role above the lowest troposphere and they argued that it could not explain why surface baroclinicity is maintained along the SST-front. This is supported by Nakamura et al. (2004), Nakamura et al. (2008) and Sampe et al. (2010) who also argued the SSHF to be the most important process for restoring baroclinicity along ocean fronts.

1.4.1 Cold Air Outbreaks

When anomalously cold air is transported over the warm ocean, and the air-sea temperature difference gets strong, we often characterize the event as a cold air outbreak (CAO) (Vavrus et al., 2006). In the literature, CAOs are often defined inconsistently. Vannière et al. (2016) explains CAOs to be generated in the vicinity of growing ECs and thereby the ECs cold sector. While Vannière et al. (2016) relates CAOs to ECs, Walsh et al. (2001) also emphasize the importance of anticyclones (high pressure systems) for pushing cold air over the oceans. Because anticyclones have the opposite rotation of cyclones, Walsh et al. (2001) argued

the high pressure systems over the North American continent to play a role for the anomalously strong cold air incursions observed over the NA. However, CAOs are not strictly confined to the mid-latitudes. In the polar regions, Rasmussen and Turner (2003) explains a CAO as cold air advection from ice-covered regions over the open ocean. A common definition for all CAOs is the existence of strong SSHF.

Chou and Ferguson (1991) investigated a CAO over the Gulf Stream region and observed significant differences in the SSHF on the cold side of the SST front compared to the warm side. The air-sea temperature difference over waters with 20°C (293 K) produced nearly twice as intense SSHF as the air-sea temperature difference over waters with 14°C (287K). In the period 1948-2008, Shaman et al. (2010) analysed the strongest events of SSHF in the Gulf Stream region. They hypothesized the intense SSHF during CAOs to potentially play a role for storm formations (cyclogenesis). Xue and Bane (1997) also found strongest SSHF during CAOs, and proposed the differential SSHF across the SST-front to increase baroclinicity and make the environment conducive for rapid growth of ECs. The thoughts of Xue and Bane (1997) are in agreement with Businger et al. (2003), who observed an intense winter storm and rapid cyclogenesis in the vicinity of a passing cold front. Businger et al. (2003) argued the enhanced air-sea temperature differences and the corresponding SSHF as a possible reason for the strong storm intensity.

1.5 Adiabatic Processes

Following Wallace and Hobbs (2006), in atmospheric science, we often distinguish between processes where a material undergo a change in its physical state with, or without, a heat exchange. The former relates back to sensible, latent and radiative heating. All these processes involve either an input or an output of heat to the environment. Such processes are also known as diabatic processes.

Following Wallace and Hobbs (2006), if a material undergoes a change in its physical state without any heat being added or withdrawn from the material, we

refer to the process as adiabatic. Adiabatic processes are related to the expansion or compression of a material when being subjected to a change in pressure. Let us consider an air parcel being displaced from a certain height z_1 to z_2, where $z_2 > z_1$. Since the pressure decreases with height, the air parcel lifted to z_2 finds itself in an environment with a lower pressure than at z_1. The air parcel will then adjust to the lower pressure by expanding. The work done on the environment then makes the air parcel cool (Wallace and Hobbs, 2006). The loss of temperature in this case is called adiabatic cooling. The opposite happens when an air parcel at z_2 moves to a region with higher pressure z_1. Instead of expanding, the air parcel will now be compressed and the temperature increases through adiabatic warming (Wallace and Hobbs, 2006).

Adiabatic processes are reversible. This means that it is possible to displace an air parcel to any level in the atmosphere and later bring it back to its original condition, as long as a change of its physical state only comes from expansion (compression) associated with a decrease (increase) in pressure (Wallace and Hobbs, 2006).

1.6 Atmospheric Stability

Because the actual temperature, T, is not a conserved quantity, we often use potential temperature, θ, instead. θ is conserved in dry adiabatic motions (Wallace and Hobbs, 2006). Because θ is conserved, the flow in adiabatic motion follows constant lines of θ (Holton and Hakim, 2012). Constant lines of θ are also called isentropes (Marshall and Plumb, 2007). Thus, in adiabatic motion, flow tend to follow isentropic surfaces.

Following (Holton and Hakim, 2012), θ can be defined mathematically as

$$\theta = T \left(\frac{p_0}{p} \right)^{R/c_p}. \tag{1.1}$$

In Eq. 1.1, T and p is the temperature and pressure at a certain height respectively, p_0 is a standard reference pressure, whereas R/c_p is called the Poisson

constant. Eq. 1.1 explains θ as the temperature a parcel of dry air would have if it was moved adiabatically to a standard reference pressure.

Following Wallace and Hobbs (2006), when θ increases with height, $\left(\frac{\partial\theta}{\partial z} > 0\right)$, the atmosphere is said to be stable. It means that if you lift an air parcel from z_1 to z_2, the air parcel finds itself in a region with warmer θ, becomes negatively buoyant and returns to its original point (z_1). In an unstable atmosphere, $\left(\frac{\partial\theta}{\partial z} < 0\right)$, θ decreases with height. If an air parcel is lifted from z_1 to z_2, it find itself in a region with colder θ and will therefore continue to rise until equilibrium is reached. In a neutral atmosphere, θ is uniform in the vertical. An air parcel will therefore remain at its place until the vertical temperature distribution changes, or the air parcel is forced to rise (sink).

1.7 Isentropic Slope

Due to the temperature differences between the Equator and the poles, isentropic surfaces must slope upwards toward colder latitudes (Hoskins et al., 2003). Slantwise ascent along isentropic surfaces, links their slope to vertical motion (Papritz and Spengler, 2015). Thus, steeper slopes would indicate the flow to have a stronger vertical component. Hoskins et al. (2003) and Papritz and Spengler (2015) defined the ascent along an isentropic surface as isentropic upglide. In relation to ECs, the isentropic upglide was shown by Hoskins et al. (2003) to be located east of the ECs. As we have already seen, the east side of an EC is related to the warm sector and the WCB. Ascending flow along an isentropic surface is therefore related to warmer air gliding upon colder air.

Papritz and Spengler (2015) interpret the slope of an isentropic surface as a proxy for baroclinicity. In this study, we follow their interpretations and define the slope in an equal way. Thus, the slope, S, can be expressed as the magnitude of the horizontal gradient of geopotential height

$$\mathrm{S} = |\nabla_\theta z|. \tag{1.2}$$

Eq. 1.2 describes the geopotential height as the height under a defined value

of θ. The magnitude of the horizontal gradient of geopotential height therefore explains the horizontal difference in height for an isentropic surface. The stronger the horizontal gradient of geopotential height is, the steeper slopes we get.

From Holton and Hakim (2012), a relationship between pressure and height exists at every column in the atmosphere, such that pressure may be used as a vertical coordinate instead of height. In this study, we have mainly used pressure as the vertical coordinate and therefore express the slope as

$$\mathrm{S} = |\nabla_\theta p|. \tag{1.3}$$

Eq. 1.3 can be modified such that the slope can be described as the horizontal gradient of potential temperature along a pressure surface. Following Papritz and Spengler (2015), expanding the total derivative of geopotential height, $p(t, x, y, \theta)$, yields

$$\mathrm{dp} = \left.\frac{\partial p}{\partial t}\right|_\theta \mathrm{dt} + \left.\frac{\partial p}{\partial x}\right|_\theta \mathrm{dx} + \left.\frac{\partial p}{\partial y}\right|_\theta \mathrm{dy} + \frac{\partial p}{\partial \theta}\,\mathrm{d}\theta. \tag{1.4}$$

With displacements only in the x- or y-direction along a constant pressure surface ($dp = 0$ and $\left.\frac{\partial p}{\partial t}\right|_\theta \mathrm{dt} = 0$), gives

$$0 = \left.\frac{\partial p}{\partial x}\right|_\theta \mathrm{dx} + \left.\frac{\partial p}{\partial y}\right|_\theta \mathrm{dy} + \frac{\partial p}{\partial \theta}\,\mathrm{d}\theta. \tag{1.5}$$

Thus, expressions for $\left.\frac{\partial p}{\partial x}\right|_\theta$ and $\left.\frac{\partial p}{\partial y}\right|_\theta$ can be given by rearranging Eq. 1.5

$$\left.\frac{\partial p}{\partial x}\right|_\theta = -\left.\frac{\partial \theta}{\partial x}\right|_p \frac{\partial p}{\partial \theta}, \tag{1.6}$$

$$\left.\frac{\partial p}{\partial y}\right|_\theta = -\left.\frac{\partial \theta}{\partial y}\right|_p \frac{\partial p}{\partial \theta}. \tag{1.7}$$

Adding Eq. 1.6 with Eq. 1.7 and expressing the horizontal gradient of p on a constant isentropic surface as $\nabla_\theta p = \left.\frac{\partial p}{\partial x}\right|_\theta + \left.\frac{\partial p}{\partial y}\right|_\theta$, yields

$$\begin{aligned}\nabla_\theta p &= -\left.\frac{\partial\theta}{\partial x}\right|_p \frac{\partial p}{\partial\theta} - \left.\frac{\partial\theta}{\partial y}\right|_p \frac{\partial p}{\partial\theta} \\ &= -\frac{\partial p}{\partial\theta}\left(\left.\frac{\partial\theta}{\partial x}\right|_p + \left.\frac{\partial\theta}{\partial y}\right|_p\right) \\ &= -\frac{\partial p}{\partial\theta}\left(\nabla_p\theta\right) \\ &= -\frac{\nabla_p\theta}{\frac{\partial\theta}{\partial p}}.\end{aligned} \tag{1.8}$$

Substituting the expression for $\nabla_\theta p$ in Eq. 1.3, with the expression in Eq. 1.8, gives an alternative definition for the isentropic slope

$$\mathrm{S} = \left|\frac{\nabla_p\theta}{\frac{\partial\theta}{\partial p}}\right|. \tag{1.9}$$

Eq. 1.9 is similar to the expression of maximum baroclinic growth from Eady (1949), who showed that the growth-rate of baroclinic cyclones not only depends on the horizontal temperature gradient, but the atmospheric stability as well. From Eq. 1.9, it can be seen that steep slopes are hardly achieved with strong atmospheric stability ($\left|\frac{\partial\theta}{\partial p}\right| >> 0$), or a week horizontal temperature gradient ($|\nabla_p\theta|$). We can also see that a strong horizontal temperature gradient and a strongly stable atmosphere are not either particularly favourable to generate steep slopes.

1.8 Slope Tendency Equation

As mentioned, Papritz and Spengler (2015) use the slope as a proxy for baroclinicity and argue that it comes with the advantage that the slope tendency is related to deformation of isentropic surfaces. Deformation of an isentropic surface would therefore indicate a change in the baroclinicity.

In this section, we derive an expression for the material tendency of the slope of isentropic surfaces. We want to separate the adiabatic and diabatic contributions with the goal to quantify the tendency they have on modifying the slope.

Following Papritz and Spengler (2015), we start by defining the vertical wind as

$$\omega = \frac{Dp}{Dt}. \tag{1.10}$$

An expansion of 1.10 in isentropic coordinates gives

$$\omega = \left.\frac{\partial p}{\partial t}\right|_\theta + \overline{U} \cdot \nabla_\theta p + \dot{\theta}\frac{\partial p}{\partial \theta}, \tag{1.11}$$

where $\dot{\theta}$ expresses the diabatic heating rate. By rearranging Eq. 1.11, an expression for $\left.\frac{\partial p}{\partial t}\right|_\theta$ can be given as

$$\left.\frac{\partial p}{\partial t}\right|_\theta = \omega - \overline{U} \cdot \nabla_\theta p - \dot{\theta}\frac{\partial p}{\partial \theta}. \tag{1.12}$$

Eq. 1.12 gives the local tendency of the height of an isentropic surface. $\overline{U} = (u, v)$ is the horizontal wind and the term $\overline{U} \cdot \nabla_\theta p$ relates the vertical component of the wind along an isentropic surface. Thus, $\overline{U} \cdot \nabla_\theta p$ is the isentropic upglide and we hereby refer to it as ω_{iu}. Because ω_{iu} yields the slantwise ascent along isentropic surfaces, it also leaves the height of isentropic surfaces unchanged (Papritz and Spengler, 2015). Thus, the change of height comes only from the deviation of the actual wind. Following Papritz and Spengler (2015), we define the deviation as isentropic displacement wind and it will hereby be referred to as $\omega_{id} = \omega - \omega_{iu}$. Equation 1.12 can now be written as

$$\left.\frac{\partial p}{\partial t}\right|_\theta = \omega_{id} - \dot{\theta}\frac{\partial p}{\partial \theta}. \tag{1.13}$$

Equation 1.13 gives the local height tendency of an isentropic surface. However, we are more interested in the local slope tendency of an isentropic surface. Remembering from Eq. 1.3, the slope of an isentropic surface can be written as $S = \nabla_\theta p$. We therefore make use of the following relationship

$$\frac{\partial S}{\partial t} = \frac{1}{2S}\frac{\partial}{\partial t}(S)^2 = \frac{1}{2S}\frac{\partial}{\partial t}(\nabla_\theta p)^2 = \frac{\nabla_\theta p \cdot \frac{\partial}{\partial t}(\nabla_\theta p)}{S} = \frac{\nabla_\theta p}{S} \cdot \nabla_\theta \left(\left.\frac{\partial p}{\partial t}\right|_\theta \right), \tag{1.14}$$

and apply $\frac{\nabla_\theta p}{S} \cdot \nabla_\theta$ to both sides of Eq. 1.13. This gives

$$\begin{aligned}
\frac{\nabla_\theta p}{S} \cdot \nabla_\theta \left(\left. \frac{\partial p}{\partial t} \right|_\theta \right) &= \frac{\nabla_\theta p}{S} \cdot \nabla_\theta (\omega_{id}) - \frac{\nabla_\theta p}{S} \cdot \nabla_\theta \left(\dot{\theta} \frac{\partial p}{\partial \theta} \right) \\
\left. \frac{\partial S}{\partial t} \right|_\theta &= \frac{\nabla_\theta p}{S} \cdot \nabla_\theta (\omega_{id}) - \frac{\nabla_\theta p}{S} \left(\frac{\partial p}{\partial \theta} \cdot \nabla_\theta \dot{\theta} + \dot{\theta} \cdot \nabla_\theta \frac{\partial p}{\partial \theta} \right) \\
&= \frac{\nabla_\theta p}{S} \cdot \nabla_\theta (\omega_{id}) - \frac{\nabla_\theta p}{S} \left(\frac{\partial p}{\partial \theta} \cdot \nabla_\theta \dot{\theta} + \dot{\theta} \cdot \frac{\partial}{\partial \theta} (\nabla_\theta p) \right) \\
&= \frac{\nabla_\theta p}{S} \cdot \nabla_\theta (\omega_{id}) - \frac{\partial p}{\partial \theta} \frac{\nabla_\theta p \cdot \nabla_\theta \dot{\theta}}{S} - \dot{\theta} \frac{\partial S}{\partial \theta}.
\end{aligned} \tag{1.15}$$

Equation 1.15 describes the local tendency to change the slope through both adiabatic and diabatic tendencies. From here, we make use of the definition of the material derivative in isentropic coordinates $\left(\frac{DS}{DT} = \left. \frac{\partial S}{\partial t} \right|_\theta + \overline{U} \cdot \nabla_\theta S + \dot{\theta} \frac{\partial S}{\partial \theta} \right)$ and express the material slope tendency equation as

$$\begin{aligned}
\frac{DS}{Dt} &= \frac{\nabla_\theta p}{S} \cdot \nabla_\theta (\omega_{id}) - \frac{\partial p}{\partial \theta} \frac{\nabla_\theta p \cdot \nabla_\theta \dot{\theta}}{S} + \overline{U} \cdot \nabla_\theta S \\
&= \text{TILT} + \text{DIAB} + \text{IADV}
\end{aligned} \tag{1.16}$$

Thus, we have three terms contributing to the material slope tendency in 1.16. The TILT-term explains the differential ω_{id}. It comes from tilting of the isentropes by upward and downward vertical wind and is related to decrease of slope through the net poleward heat transport. Papritz and Spengler (2015) found the TILT-term to climatologically compensate the diabatic tendencies.

The IADV-term in Eq. 1.16 is the isentropic advection. The sum of TILT and IADV gives the adiabatic contributions of the slope tendency equation (Papritz and Spengler, 2015).

The DIAB-term yields the material slope tendency from differential diabatic heating. Papritz and Spengler (2015) showed the time and zonally averaged DIAB-term in the NA (80°W to 0°E) to be a maximum around 40°N. Furthermore, they found the DIAB term to be particularly strong between 700 and 500 hPa and explained the strong values of DIAB around 40°N to be a result of intense LH above the warm waters of the Gulf Stream.

1.8.1 Impact of LH on the Isentropic Slope

Fig. 1.4 illustrates how LH-release lowers the isentropic surface at the point of the heating, causing a decrease in the slope on the left hand side (LHS) of the heating maximum and an increase in slope on the right hand side (RHS).

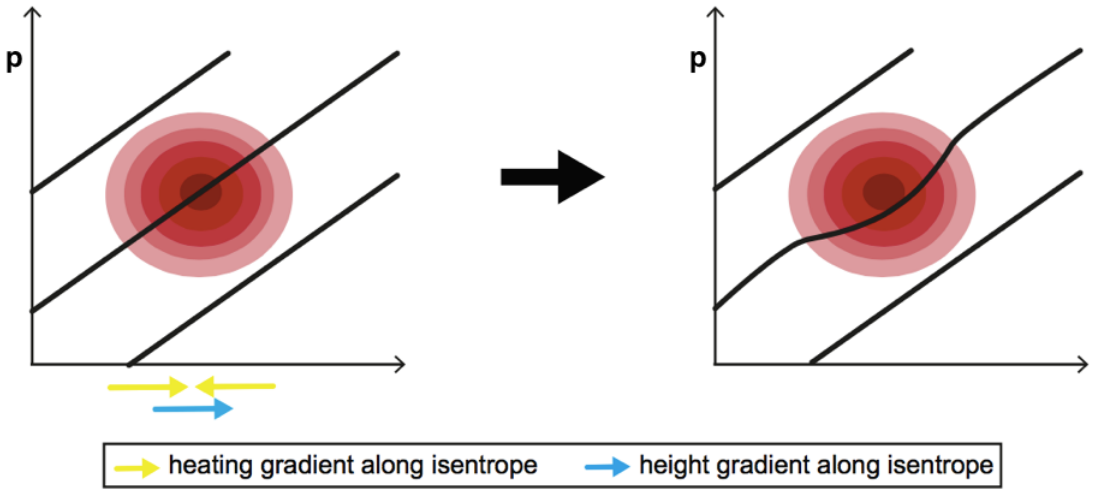

Figure 1.4: Figure adapted from (Papritz and Spengler, 2015), showing an illustrative example of how LH modifies an isentropic slope. Maxima LH is indicated by darkest red shadings. Black contours are isentropic surfaces.

This is consistent with the mathematical expression of slope tendency from diabatic heating (DIAB in Eq. 1.16). At the point of the LH-release (Fig. 1.4), maximum values are seen in the center, with decreasing values toward the edges. Thus, the heating gradient (yellow arrows) on the RHS of the heating maximum is opposite to the heating gradient on the LHS of the heating maximum. Because the height gradient (blue arrow) is in the same direction as the heating gradient on the LHS, it comes from Eq. 1.16 that when $\nabla_\theta p > 0$ and $\nabla_\theta \dot{\theta} > 0$, the slope decreases through diabatic processes, but when $\nabla_\theta \dot{\theta} < 0$, the slope increases. Because $\nabla_\theta \dot{\theta} < 0$ at the upslope side of the heating maximum, we see an increase of slope there, while $\nabla_\theta \dot{\theta} > 0$ on the downslope side, which results in a decrease in slope. Considering the case of Fig. 1.4, the atmosphere is uniformly stable, such that a net increase in the isentropic slope does not occur. This is owed to the

fact that the slope on the downslope side is reduced with the same magnitude as the slope is increased on the upslope side.

However, if the atmosphere is not uniformly stable, a net increase of slope may occur. For instance, if the stability is weaker on the RHS of the heating maximum compared to the LHS, the upslope side will have a greater increase in slope than the decrease of slope on the downslope side. If this is the case, we may experience a net increase of slope.

In addition, the LH-release makes the atmosphere more stable below the heating (isentropes closer together) and more unstable aloft (isentropes further apart). The opposite response happens during a cooling event (evaporation). During evaporation, the atmosphere will be more stable above the cooling and less stable below. However, both processes (condensation and evaporation) will tend to make the atmosphere more unstable around the maximum heating or cooling. As can be seen in Eq. 1.9, a more unstable atmosphere may give steeper isentropic slopes. It is for this reason Papritz and Spengler (2015) argue that consistent diabatic heating, or cooling, will have a net increase on the slope.

1.8.2 Impact of SSHF on the Isentropic Slope

When considering how SSHF modify the slope, we pay more attention to the isentropes closer to the surface (Fig. 1.5). Similar to the LH-case (Fig. 1.4), we still consider a stable atmosphere. The height gradient indicates a horizontal temperature gradient with warmer θ on the left than on the right. This leads to differential SSHF with strongest values on the LHS (yellow arrow) The strongest SSHF (red arrows) provide heat to the overlying air, making the isentropes warmer. The heating by the SSHF intersects the original isentrope to the right, increasing the horizontal temperature gradient. Moreover, because the SSHF are stronger on the LHS than on the RHS, they bend the isentropes in a manner that increases the slope. As we see from Fig. 1.5, the slope response from SSHF is mainly confined to the lower troposphere.

The increase of slope from SSHF is consistent with the DIAB-term in Eq. 1.16. In Fig. 1.5, $\nabla_\theta p > 0$ and $\nabla_\theta \dot{\theta} < 0$, which leads to an increase in slope.

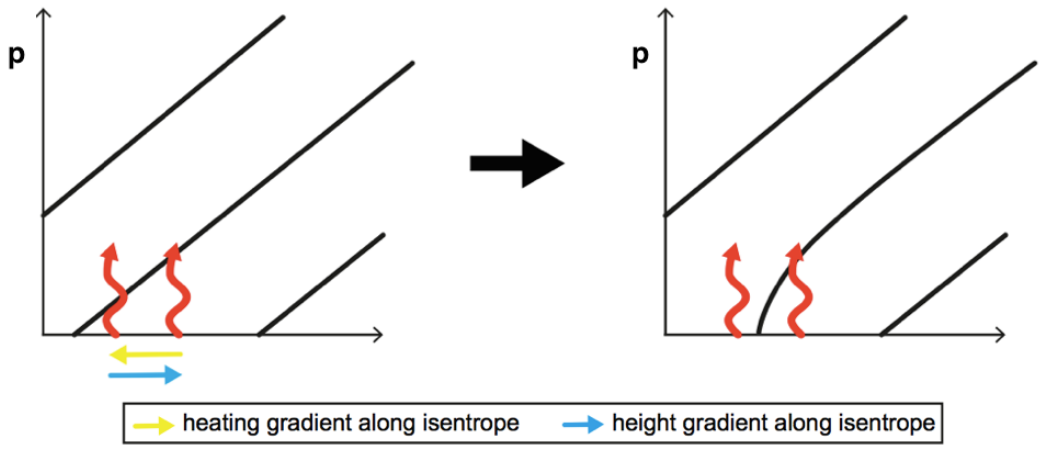

Figure 1.5: Figure adapted from (Papritz and Spengler, 2015), showing an illustrative example of how SSHF modify an isentropic slope. Black contours are isentropic surfaces. Maximum upward directed SSHF are indicated by red curly arrows.

1.9 Hypothesis

The uncertainty of what actually causing the NA storm track to collocate with the SST-front has lead to a numerous amount of studies (e.g., Hoskins and Valdes, 1990; Hotta and Nakamura, 2011). There is considerable agreement that the total diabatic heating is the main reason for restoring baroclinicity along the SST-front, but if the diabatic heating from LH or from SSHF play the most dominant role is still up for discussion.

What we hypothesize is schematically illustrated in Fig. 1.9. Let us imagine an idealized EC, collocated with the meridional SST-front as seen in a). The warm sector of the EC pushes air from the south towards the SST-front. When the air hits the steeper slopes, it starts to rise. The isentropic upglide (red arrows) brings moisture from the surface, to the upper levels, triggering cloud formations and subsequent LH-release. On the opposite side, the cold sector of the EC advects cold air from the north. On its way to warmer regions, the air descends and accumulates over the warmer ocean. This leads to a large air-sea temperature difference and subsequent strong SSHF.

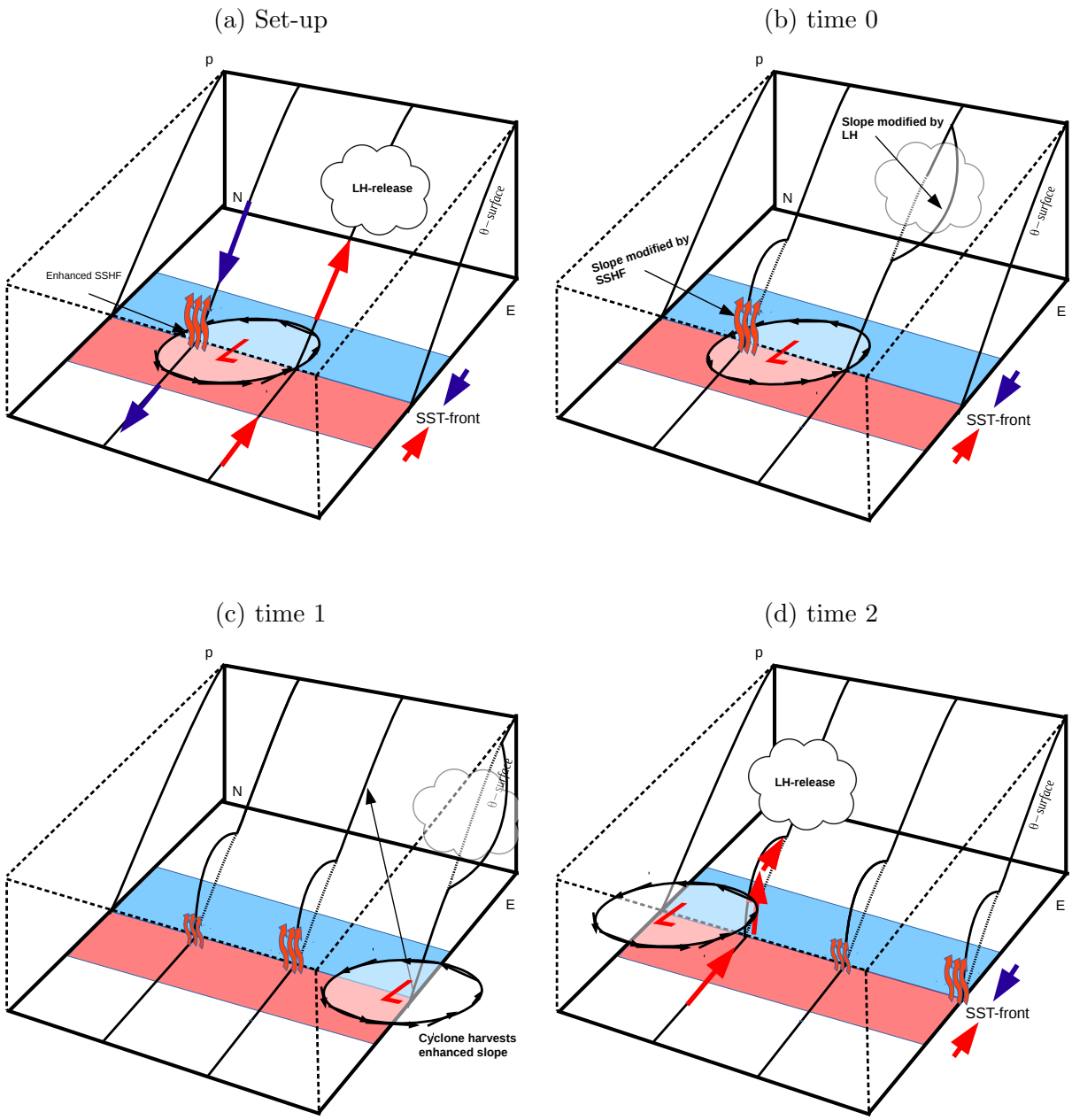

Figure 1.6: Schematic illustration of how ECs potentially maintain baroclinicity along the SST-front. Straight red (blue) arrows show isentropic upglide (downglide) and upward directed curly arrows indicate SSHF. The isentropic surface (black lines) slopes upward toward colder regions. a) shows the initial set-up, without modification of slope, b) shows the initial set-up with modification of slope, c) shows slope response when the EC propagate eastwards and d) illustrates the next EC entering the box.

In b), we illustrate how SSHF and LH potentially modify an isentropic surface in the same set-up as in a). Similar to what was explained theoretically in Fig. 1.4 and Fig.1.5, LH-release lowers the isentropic surface at the point of the heating (cloud) in b). Thus, around the point of the LH-release, we see a decreased slope south of the cloud and increased slope north of the cloud. In this case, we hypothesize the slope to increase more north than it decreases south. The LH-release therefore generates a net increased slope.

In the cold sector, an increase of slope can be seen due to the differential SSHF across the SST-front. The warm side of the SST-front provides more heat to the overlying layer, steepening the slope at this point. This bends the isentropes similarly to what we saw in Fig. 1.5.

As the EC propagates east along the SST-front (in c)), it enters the self-induced baroclinicity from the LH-release. The EC harvests the increased slope in this region, such that it retains intensity and the upper slope returns to its original position. The increased slope from the SSHF still remains untouched, because it is in the vicinity of the EC. As the EC travels along the SST-front (in c)), it also advects the cold and warm sector further east. Thus, similar modifications of the slope can be seen downstream of the EC's original position in b). In d), the EC has moved outside the box and again harvested the increased slope from its own LH. The increased slope from the SSHF is still untouched and can now be seen throughout the box. Thus, when the next EC enters the box from the western side, it meets the increased slope in the lower levels and starts to push warm air towards the steep isentropes, which again triggers LH-release.

Hence, we hypothesize that both the warm and cold sector of an EC collaborate for restoring baroclinicity along the SST-front. We think that, through LH-release, the warm sector play a role for fuelling already existing ECs, while the cold sector makes the environment conducive for the next ECs to release LH via isentropic upglide.

The remaining part of this study is divided into four chapters. In chapter 2, we present the dataset. A presentation of the performed methods follows in the next chapter (3). In chapter 4, we investigate the relationship between LH and SSHF in

the Gulf Stream region. An extra attention is given to the 10 % strongest events of SSHF and LH, because we think they could represent ECs travelling along the SST-front. In the final chapter of this study (5), we present some concluding remarks.

Chapter 2

Data

2.1 Year of Tropical Convection

The Year of Tropical Convection (YOTC) was a meteorological field campaign, initiated by the World Climate Research Programme and the World Weather Research Programme, with aim to improve the understanding of tropical convection (World Meteorological Organization, 2008). The National Center for Atmospheric Research (2016) describes the YOTC-campaign as a coordinated initiative among scientists to collect huge amounts of available observations, use the observations in advanced atmospheric models and produce high resolution operational datasets. The datasets could then be used for research and to improve forecasts of tropical convection. The YOTC-campaign also intended to advance the understanding of how weather in the tropics interacts with weather in the extratropics (The National Center for Atmospheric Research, 2016).

2.2 Data

In this study, we take all data from the European Center for Medium Range Forecasting (ECMWF) during the YOTC-period (1st of May 2008 to 30th of April 2010). The fields we investigate are global analyses (sea level pressure, skin temperature, winds etc.) and short range forecasts of SSHF. In addition, we use a set

of temperature tendencies that are given by the available physics schemes.

The data are produced by ECMWF's own atmospheric model known as the Integrated Forecasting System (IFS). Following ECMWF (2015), the dynamical core of the IFS is hydrostatic, semi-implicit and semi-lagrangian. In the period 1st of May 2008 to 26th of January 2010, the horizontal resolution of the IFS model was 25 km. For the remaining period, the horizontal resolution increased to 16 km.

IFS apply a 4D-variational data assimilation (4D-var) method (ECMWF, 2015). From Warner (2011), 4D-var combines a previous forecast with available observations and optimizes the forecast sequentially by looking at the spread between the forecast output at a certain time step and the observations at the same time step.

Following ECMWF (2015), the small scale physical processes (sub-gridscale physical processes) in the IFS, that cannot be resolved for the model's horizontal grid size, need to be approximated through a set of already known quantities. This is called parametrization. For the YOTC-period, the physical parametrizations in IFS provide the sub-gridscale temperature tendencies dealing with radiation, clouds, deep and shallow convection, sub-gridscale turbulence and sub-gridscale orography.

The global analyses are available four times a day (00, 06, 12, 18 UTC) and the short range forecasts are run once daily at 12 UTC. The forecast fields are obtained and averaged from the forecast both 3 hours before and after the desired time. For instance, the forecast fields at 06 UTC are derived from the averaged fields at 03 UTC (15 hours lead time) and 09 UTC (21 hours lead time).

In this study, we use the following 13 pressure levels (hPa) : 1000, 950, 925, 900, 800, 700, 600, 500, 400, 300, 250, 200. We only use data from the two winter seasons during the YOTC-period (December, January and February (DJF) 2008-2010). In total, we therefore include 720 time steps in our calculations. All fields are interpolated on a 0.5° x 0.5° grid.

Chapter 3

Methods

3.1 Choice of Region

In this study, we investigate how SSHF and LH maintain baroclinicity in the Gulf Stream and along the corresponding SST-front. We therefore find it reasonable to limit our research to only cover the part where the SST-gradient is strongest. We saw in Fig. 1.2 that the strongest SST-gradient started in the mid-latitudes and elongated zonally from the east coast of the US, towards approximately 50°W. East of 50°W, the strong SST-gradient started to tilt northwards.

We decide to focus on the region with the most zonally aligned isotherms and the strongest confined meridional SST-gradient. Because the meridional SST-gradient is strongest around 40°N, we create a symmetric box to cover the latitudes of 30°N to 50°N and the longitudes of 70°W to 50°W. A new figure of the SST-gradient, with the box attached, can now be seen in Fig. 3.1. The strong SST-gradient inside the box is therefore the region of strongest focus and will be referred to as the Gulf Stream region.

The tilted strong SST-gradient east of 50°W is not included in this study, partly because this simplifies the calculations and makes interpretations of data less complicated. The main reason though, is because recent studies have shown the NA storm track to show strongest sensitivity to the SST-gradient covered by the box. For instance, Small et al. (2014) smoothed the SST-gradient in one of their

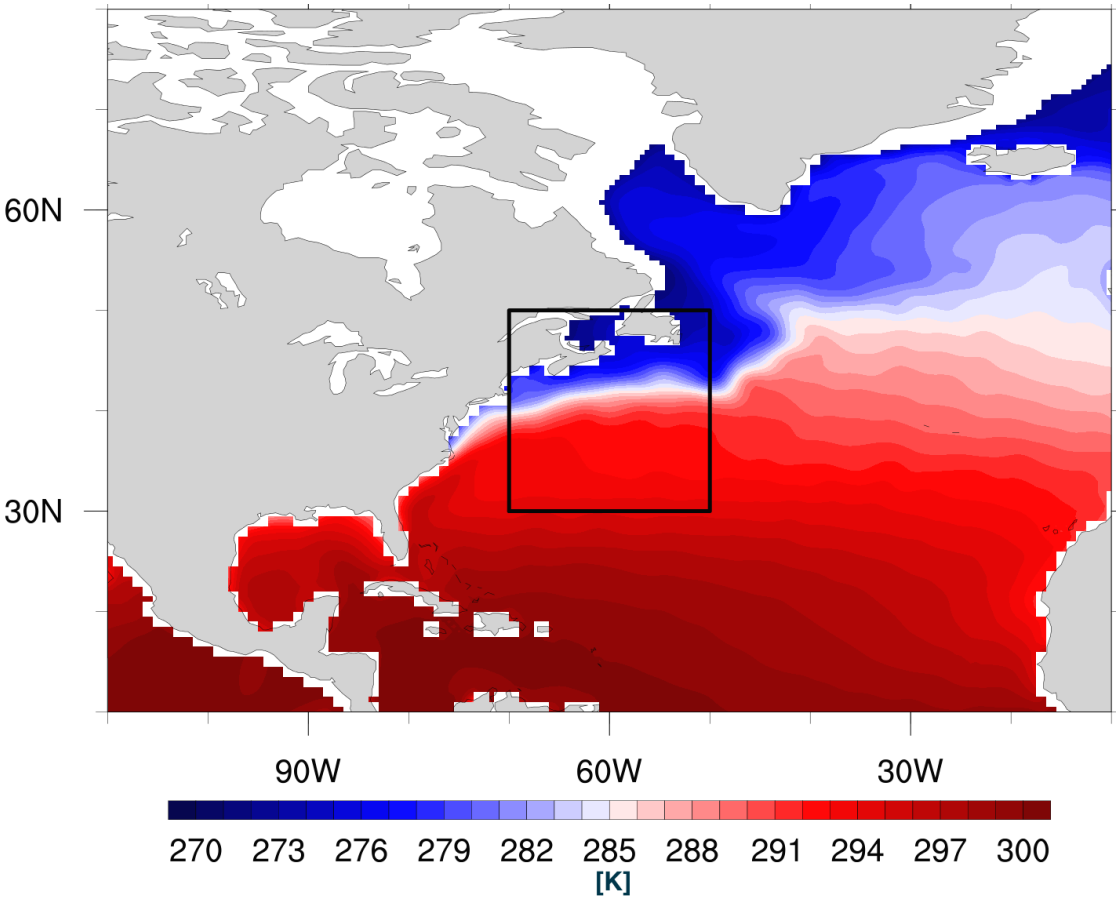

Figure 3.1: Time averaged sea surface temperature (K) for DJF. The area depicted is 110°W to 10°W and 10°N to 80°N. Temperatures on land and ice-covered regions are not included. Box is centred over the meridional SST-gradient for the Gulf Stream region (70°W to 50°W and 30°N to 50°N).

high resolution runs and showed the NA storm track to be most sensitive to the meridional part of the SST-gradient. The same was observed by Woollings et al. (2010), who also discovered the NA storm track to be most affected by the SST-gradient covered by the box. In addition, other studies have discovered intense LH-release in the box region (e.g., Minobe et al., 2008; Papritz and Spengler, 2015), as well as strong SSHF in relation to a CAO (e.g., Chou and Ferguson, 1991; Businger et al., 2003).

3.2 Slope Tendency from LH

In section 1.7, we explained that the slope of an isentropic surface could be used as a proxy for baroclinicity, such that a modification of the slope was analogous to a change in the baroclinicity. If we remember back to Eq. 1.15, the DIAB-term, $\frac{\partial p}{\partial \theta}\frac{\nabla_\theta p \cdot \nabla_\theta \dot{\theta}}{S}$, comprised the total slope tendency from diabatic heating, where $\dot{\theta}$ yielded the diabatic heating rate. For the YOTC-period, the diabatic heating rate arises from the available temperature tendencies mentioned in section 2.2. Following (Papritz and Spengler, 2015), the total diabatic heating rate can be given as

$$\begin{aligned}\dot{\theta} = & \frac{\theta}{T}\left(\frac{\partial T}{\partial t}_{rad} + \frac{\partial T}{\partial t}_{cloud} + \frac{\partial T}{\partial t}_{dsc} + \frac{\partial T}{\partial t}_{tur} + \frac{\partial T}{\partial t}_{oro}\right) \\ & = \dot{\theta}_{rad} + \dot{\theta}_{cloud} + \dot{\theta}_{dsc} + \dot{\theta}_{tur} + \dot{\theta}_{oro},\end{aligned} \tag{3.1}$$

where the temperature contributions treating clouds, together with deep and shallow convection, give the temperature tendency from LH as

$$\dot{\theta}_{cloud} + \dot{\theta}_{dsc} = \dot{\theta}_{LH}. \tag{3.2}$$

The total slope tendency from LH is given by investigating $\dot{\theta}_{LH}$ in the DIAB-term (Eq. 1.15). Because we in this study look at the slope response from LH and SSHF, the slope tendency from LH will be used to investigate the former. The SSHF are represented in the $\dot{\theta}_{tur}$, but not explicitly. For this reason, we cannot investigate the direct slope tendency from SSHF.

3.3 Calculations

We use CDO (2016) to extract the box region from the global dataset (see box in Fig. 3.1). Because we are mainly interested in the values from the ocean and the ocean front, the land areas that penetrate the northern edge of the box are excluded, if not stated otherwise.

We use The NCAR Command Language (2015) to produce the figures in this study. Time and horizontal averages are calculated with the help from CDO

(2016).

3.3.1 Horizontal Climatologies

For the horizontal climatologies, we take the time average of the two winter seasons DJF for the latitudes of 10°N to 80°N and the longitudes of 110°W to 10°W. We overlay the box from Fig. 3.1 to all the horizontal climatologies as a method to compare the overall distribution in the NA, to the distribution inside the box. However, for the horizontal climatologies, no additional calculations are performed inside the box.

For the variables that are not confined to the surface, we vertically integrate them before taking the time average.

3.3.2 Vertical Cross Sections

The vertical cross sections in this study are time and zonally averaged for the two winter seasons (DJF) inside the box for the 13 different pressure levels introduced in chapter 2. It is thus possible to compare how the different variables are distributed in the vertical, as well as getting a more lucid view on how the values in the box are displaced across the strong SST-gradient.

In addition, we attach the time and zonally averaged SST to the bottom part of the figures. We furthermore shade the overlaying isentropes in the same color as the color representing the SST. With this method, we see more clearly the meridional distribution of the air-sea temperature differences in the box and across the SST-front.

3.3.3 Vertical Cross Correlations

From Emery and Thomson (2001), the correlation coefficient r is a non-dimensional number between -1 and +1, where -1 determines the variables to be out of phase and +1 determines the variables to be in phase. If $r = 0$, the variables are not related to each other. The cross correlation yields the correlation coefficient

between two or more variables, where one variable is lagged with respect to the others.

In this study, we create cross correlations of all available time steps for DJF inside the box. We use a lag time of 48 hours back and forward in time, with a 12 hour interval. We plot the cross correlation at all 13 available pressure levels up to 200 hPa. We do this to see if there are any lagged response from one variable to another.

We find the lagged correlation coefficients with the built in function "esccr" from The NCAR Command Language (2015).

3.4 Composites

We create composites by taking the zonal and meridional mean of a desired variable, i.e. LH, for all available time steps inside the box. The zonal and meridional mean values give the time series of LH inside the box. Furthermore, we use CDO (2016) to pick out the 10 % highest values of all the time steps in the time series. The 10 % highest values of LH are then equivalent with the 90^{th} percentile LH.

Because the whole time series consists of 720 time steps, the 90^{th} percentile returns the 72 strongest values of LH. We want to avoid using the same events more than once and extract only the peak values of consecutive time steps. For instance, if the time steps suddenly jump forward in time, we identify the jump as a distinction between two strong events.

From here, we identify the time of the peak values and use these time steps to extract data from a different variable, i.e isentropic slope. We then take the time average of the extracted isentropic slope and composite it with respect to the strongest LH. This leaves us with information about how the isentropic slope behaves during the time steps for the 90^{th} percentile LH. We composite the isentropic slope on a greater spatial domain (110°W to 10°W and 10°N to 80°N) than just the box region (where LH was strongest). We therefore obtain the large scale picture of how slope and LH correspond. We furthermore lag the composites 48 hours back and forward in time, with a 12 hour interval. The lagged composites

may therefore expose the temporal evolution of the isentropic slope when the LH has peak values.

In addition to the strong LH-events, we also create composites from the 90^{th} percentile slope tendency from LH, as well as the SSHF. For the latter case, the amount of peak time steps are moderate (table 3.1). We checked the 80^{th} percentile SSHF and observed only ten additional peak time steps. We considered to investigate the 80^{th} percentile instead, but decided to stick with the 90^{th} percentile SSHF, because this study is most interested in the extreme events. We see from table 3.1 that the total number of peak time steps for the 90^{th} percentile LH and slope tendency from LH are higher than for the SSHF. Thus, the analyses are more robust for the two former cases.

Variable	Total time steps	90^{th} percentile	Peak values
LH	720	72	30
Slope tendency from LH	720	72	31
SSHF	720	72	16

Table 3.1: Peak values for the 90^{th} percentile of LH, slope tendency from LH and SSHF inside the box.

3.4.1 Detecting Cold Air Mass

We use a a diagnostic from Iwasaki et al. (2014) to detect CAOs. They define a cold air mass (CAM) by taking the difference between the atmospheric pressure at the θ_{280K}-level and the atmospheric pressure at the surface: $DP = P_s - P_{\theta_{280K}}$. The difference gives a measure of the deepness of the air column below θ_{280K}. A deep CAM is thus a signal of cold air, and intrusion of deep CAM into a region could therefore indicate a CAO.

Iwasaki et al. (2014) showed the airmass below θ_{280K} to be an accurate measure of CAM into the mid-latitudes. At around 45°N in the NH, Iwasaki et al. (2014) found the θ_{280K} to be the height where the cold and descending polar air started to move with a more equatorwards component. Thus, detecting the meridional

component of the CAM could indicate a CAO in the mid-latitudes. Iwasaki et al. (2014) tested other threshold values and argued the θ_{280K} to be the threshold that best represented the movement of the CAM toward lower latitudes. For instance, with θ_{290K} as a threshold, the position of the CAM shifted south and got displaced beyond the subtropical yet. For this reason, the movement of the CAM propagated more eastwards, and the meridional intrusion of cold air got more difficult to detect. With θ_{270K} as a threshold, the position of the CAM got displaced further north and was mainly confined to the high latitudes. CAM into the mid-latitude was therefore more difficult to detect.

We adapt the method of Iwasaki et al. (2014) and use the θ_{280K} as a threshold when compositing the CAM in response to the 90^{th} percentile LH and SSHF.

3.4.2 Potential Vorticity

From Holton and Hakim (2012), an upper level low pressure system, usually called an upper level trough, is associated with warm air above the trough and cold air below. An upper level trough is often characterized as a tropopause fold, owed to the fact that the low pressure and the cold air below lowers the height of the tropopause. Cyclonic movement of the wind is also associated with an upper level trough.

One way to characterize upper level troughs are through the detection of upper level positive potential vorticity (PV) anomalies. Above an upper level positive PV anomaly, the isentropes bulge downwards. Below the positive PV-anomaly, the isentropes bend upwards. In a stable atmosphere (θ increases with height), upward bending of the isentropes at the surface is associated with colder air below the lifted isentropes.

In this study, we use the PV at the θ_{320K} isentropic surface, where θ_{320K} is meant to represent the upper troposphere. If we observe strong upper level positive PV anomalies in the mid-latitudes, they could indicate an upper level trough and possibly a CAO. We composite the PV at θ_{320K} for the 90 th percentile LH and SSHF.

3.4.3 Detecting Cyclones

We use a cyclone track to identify regions that are highly influenced by cyclones and cyclogenesis. The cyclones are identified as minima in sea level pressure inside the outermost closed isobars. We attach them as white dots onto the composites. The cyclogenesis are defined as the time when a cyclone first appears. We attach cyclogenesis events as white dots with a purple ring onto the composites.

Chapter 4

Results

4.1 Climatological View on the North Atlantic and the Gulf Stream Region

In Fig. 4.1, we present the spatial distribution of the isentropic slope in the NA and show that it has the strongest values inside the box. Because the slope is the ratio between the horizontal temperature gradient and the atmospheric stability (Eq. 1.9), the steepest slopes coincides with where we have the strongest SST-gradient (Fig. 3.1). In addition, the box region, and thereby the Gulf Stream region, is well known for frequent CAOs (e.g., Walsh et al., 2001; Shaman et al., 2010), which tend to destabilize the atmosphere (Stull, 2001).

The steep slopes in the Gulf Stream region make the region conducive for consecutive cyclogenesis. If we assume frequent intrusion of ECs inside the box, we also assume steady warm air advection, from the ECs warm sector, toward the steeper slopes (Fig. 4.1). Because the temperature gets colder when moving north, the isentropes must slope upwards toward higher latitudes (Hoskins et al., 2003). If we move from south to north inside the box, the slope starts to steepen strongly on the warm side of the SST-gradient (Fig. 4.1). There seems to be a rapid steepening from 35°N to 45°N and a more moderate steepening north of 45°. Thus, when the warm and humid air from the ECs warm sector meets the steeper isentropic surfaces, the air starts to ascend and is capable of triggering LH-release.

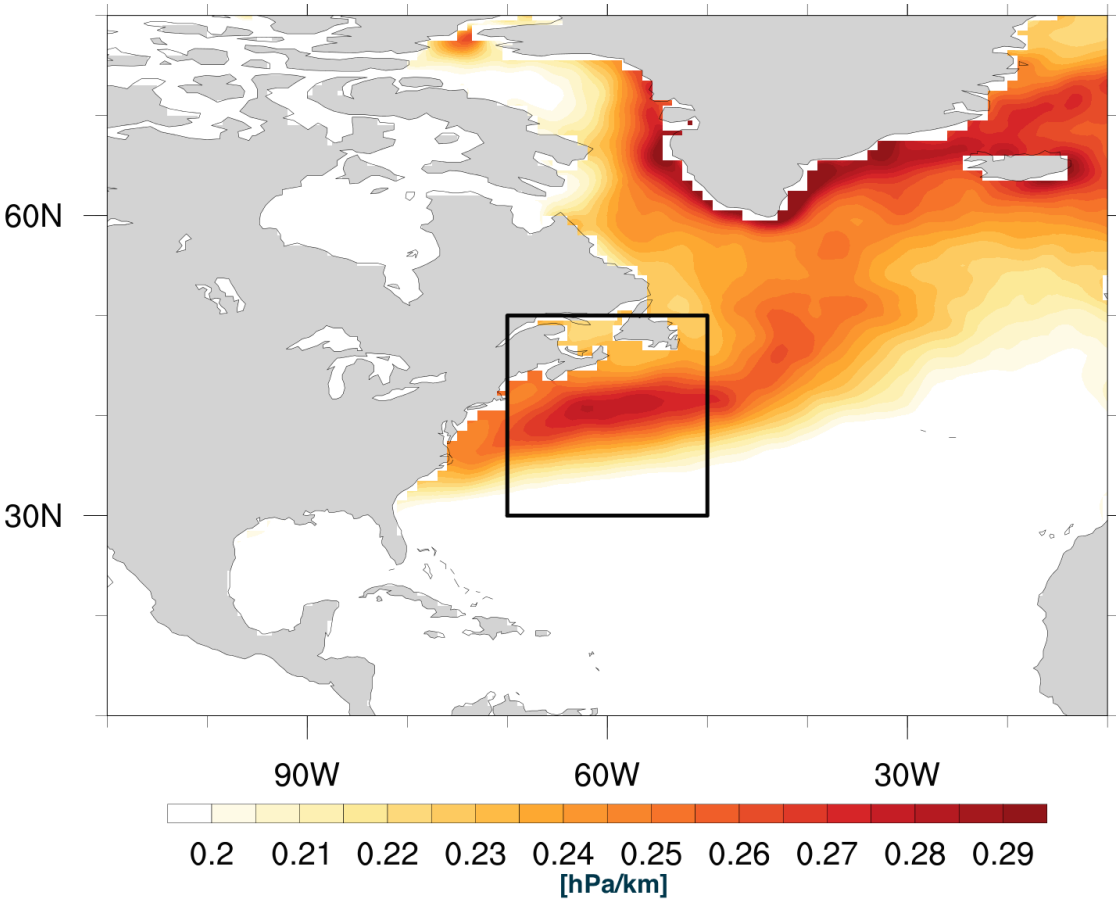

Figure 4.1: Time averaged, vertically integrated (1000-200 hPa) isentropic slope (hPa/km). Values of slope over land and slope below 0.2 hPa/km are not included. The box is similarly attached as in Fig. 3.1.

We therefore expect strong isentropic upglide along these steep slopes. Because the slope starts to steepen on the warm side of the SST-gradient, the spatial distribution of the strongest LH also starts to have positive values around this point (Fig. 4.2a). Maximum LH seems to coincide with the steepest slopes (Fig. 4.1), probably because of strong isentropic upglide prior to the LH-maximum.

Regarding the slope tendency from LH (Fig. 4.2b), the response is similar inside the box as it is for the LH (Fig. 4.2a). Since the values are positive, they indicate that LH-release acts to increase the slope, which is implied in our hypothesis (section 1.9) and also shown by Papritz and Spengler (2015). An important remark

is to remember that only the tendency to change the slope from LH is investigated. Even though it shows strong positive values inside the box, the total change of slope may not be increasing due to the reduction of baroclinicity, related to the ECs net poleward heat transport. As we mentioned in section 1.8, Papritz and Spengler (2015) showed the TILT-term in Eq. 1.15 to climatologically compensate the diabatic heating tendencies. That being said, the strong positive values of slope tendency from LH inside the box, indicate the LH-release to have a positive contribution to change the slope.

The climatologies of LH (Fig. 4.2a) and slope tendency from LH (Fig. 4.2b) capture the horizontal distribution in the box, but leaves us uncertain of how LH and slope tendency from LH are distributed in the vertical. We therefore present time and zonally box averaged vertical cross sections of LH and slope tendency from LH in Fig. 4.3.

For the vertical distribution of LH (Fig. 4.3a), we see that the evaporation is confined to the lowest levels and the condensation begins at approximately 900 hPa. The two different regimes (evaporation and condensation) are the reason for why the vertical integrations of LH and slope tendency from LH (Fig. 4.2a, 4.2b) are taken from 900-200 hPa, and not 1000-200 hPa, as we did for the slope (Fig. 4.1). Because this study mainly focuses on the slope response from condensation, we decided to separate the processes. We suspected that the slope response from condensation would be partly cancelled if we included the vertical layers that were dominated by evaporation. Because we excluded the lowest vertical levels in the integration of LH, we found it reasonable to do the same for the tendency from LH.

The strongest condensation in Fig. 4.3a seems to be centred between 900-400 hPa, with a maximum at a relatively shallow layer between 900-800 hPa. The maxima is also where we see the steepest isentropes, and we therefore expect strong isentropic upglide here. The strong isentropic upglide potentially triggers strong LH-release and may explain the reason for the maximum values of LH between 900 and 800 hPa.

(a) LH

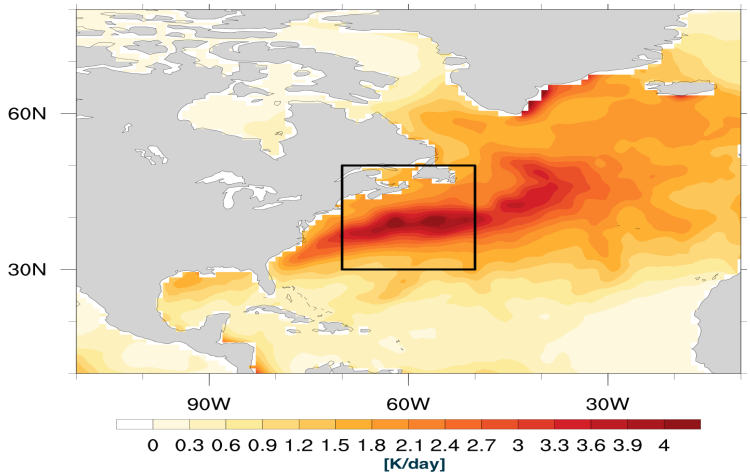

(b) Slope tendency from LH

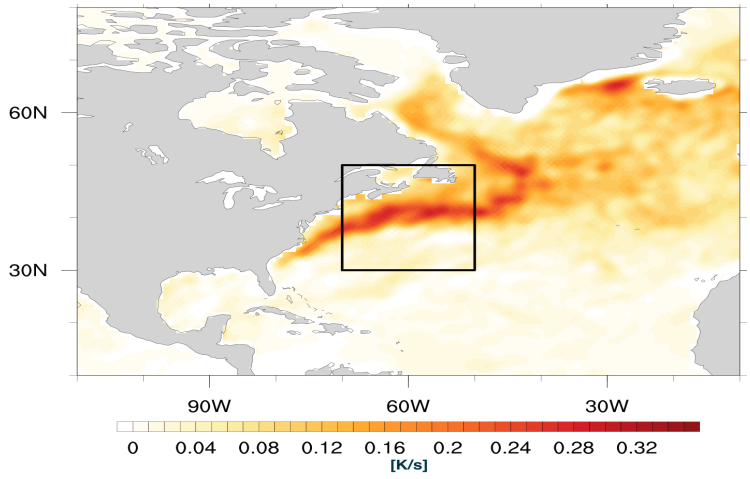

(c) Surface Sensible Heat Fluxes

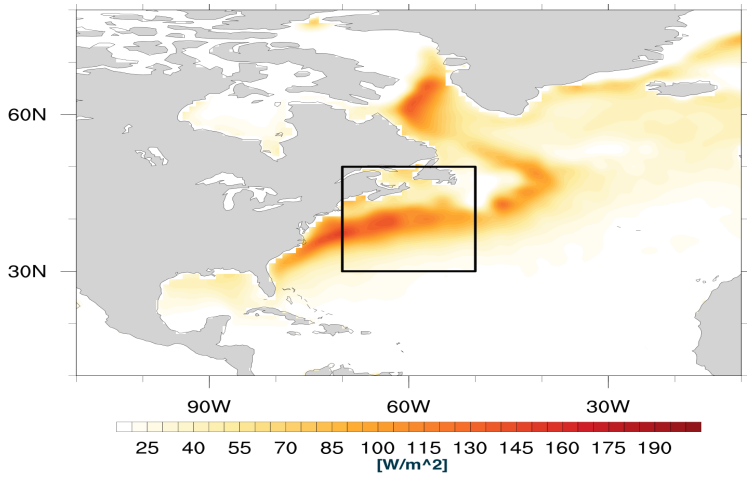

Figure 4.2: Time averaged, vertically integrated (900-200 hPa) LH (*Kelvin per day*) in a), vertically integrated (900-200 hPa) slope tendency from LH (*Kelvin per second*) in b) and SSHF (W/m^2 in c). Values over land are not included.

In addition, Fig. 4.3a shows large air-sea temperature differences in the lowest vertical levels. For instance, at around 40°N, the $\theta_{SST} - \theta_{850hPa}$ exceeds 2K. Papritz et al. (2014) characterized a CAO as when the $\theta_{SST} - \theta_{850hPa}$ exceeded 4K. Because Fig. 4.3a is a two winter season climatology and still have large air-sea temperature differences, these regions probably generate strong turbulent fluxes. The turbulent fluxes transport heat and moisture from the ocean to the atmosphere, and when the warmer air gets in contact with the cold overlying air, the water vapour may condense and release LH to the environment. We therefore expect the turbulent fluxes, together with the steep isentropes, to have an impact for the maxima LH-release around 900-800 hPa. The LH-release is weaker in the upper troposphere, which probably has to do with the more gentle slopes and the fact that the turbulent fluxes are more moderate here.

Regarding the vertical cross section for the slope tendency from LH (Fig. 4.3b), maximum values are slightly shifted towards the north, compared to the maximum values of LH (Fig. 4.3a). If we remember back to section 1.8.1, we explained that LH-release lowers the isentropes at the point of the heating, leading to a decrease in slope on the downslope side of the LH maxima and an increase of slope on the upslope side.

We can interpret from Fig. 4.3b that we have positive values of slope tendency from LH on the upslope side of the LH-maxima in Fig. 4.3a. The positive values indicate that there is a tendency for LH to increase the slope. Again, we must emphasize that we only see the slope tendency from LH and not the total slope tendency (see Eq. 1.15). That being said, similar to the horizontal distribution of the slope tendency (Fig. 4.2b), positive values indicate that there is a contribution from LH to increase the slope. This is what we implied in section 1.9 and we will follow this up in the upcoming sections.

(a) LH

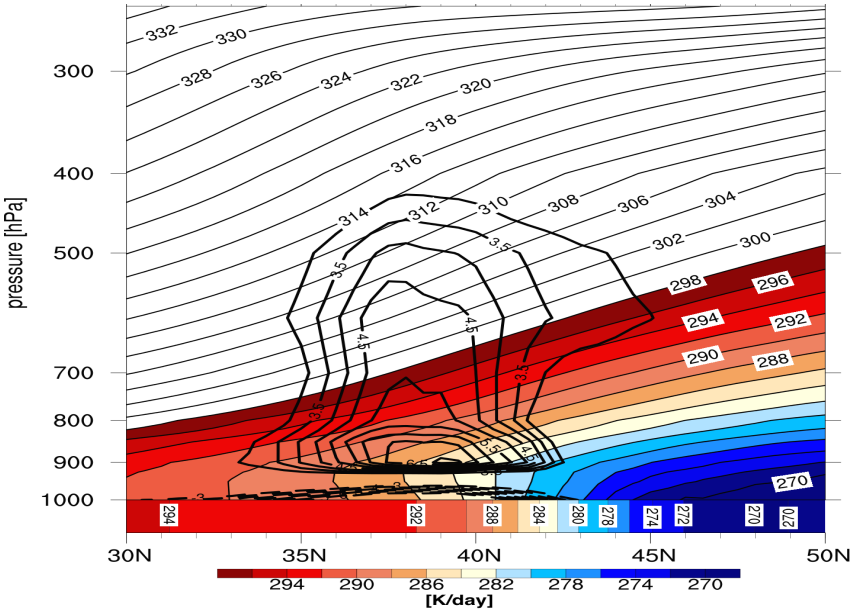

(b) Slope tendency from LH

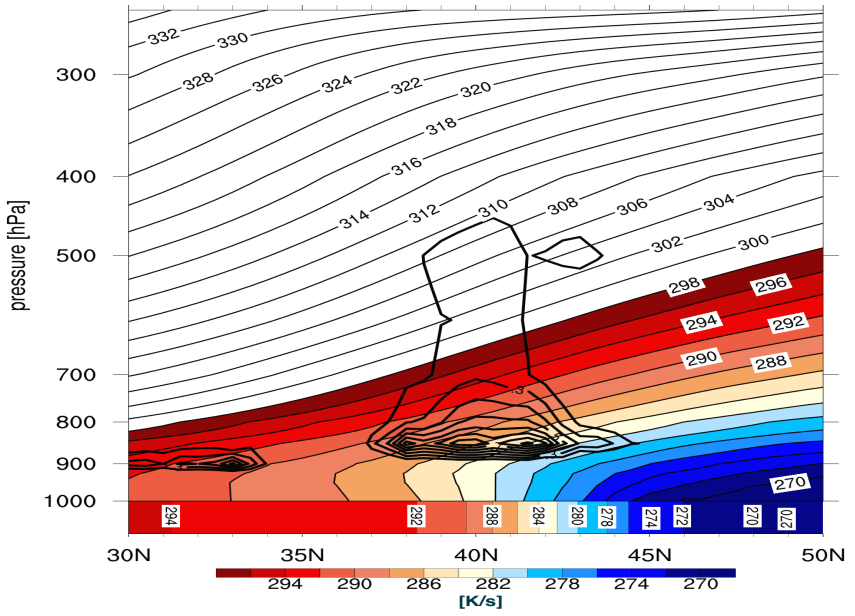

Figure 4.3: Vertical cross section for the time and zonally averaged LH (K/day) in a) and slope tendency from LH (K/s) in b). The region depicted is inside the box (70°W to 50°W and 30°N to 50°N). In a) dashed lines show evaporation while solid lines show condensation. In b) solid lines show positive slope tendency from LH. Attached is the corresponding SST. The lowest tropospheric θ-lines are shaded in the same colors as the SST

Up to now, we have shown the box to be a region with a strong meridional SST-gradient, steep isentropic slopes, strong LH-release and large air-sea temperature differences close to the surface. The latter are likely to generate strong SSHF as well. By looking at Fig. 4.2c, we see indeed strong SSHF along the SST-gradient. However, maximum values are partly shifted outside the box and can be seen close to the North American continent. Because we expect the air to be coldest immediately after leaving land, the air-sea temperature differences are probably also largest close to the continent. The eastern side of the box is further away from the land, meaning that the air-sea temperature difference here is probably smaller, which produces less intense SSHF.

Compared to the LH (Fig. 4.2a), maximum values of SSHF are in general displaced more to the west (4.2c). If we assume the box to be frequently invaded by ECs, it is reasonable to believe that the strongest SSHF (generated by the ECs cold sector) would be in the vicinity of the strongest LH (generated by the ECs warm sector).

A final remark is that the strongest SSHF seem to be slightly shifted to the warm side of the SST-front. When cold air comes in from the North American continent, a larger air-sea temperature difference is generated on the warm side of the SST-front, thus strongest SSHF are also seen here.

4.2 Comparison of Intense LH- and SSHF-events

In this section, we present a synoptic analysis of the 10% highest values (90^{th} percentile) for LH and SSHF (see detailed information in the method section 3.4). The former is first vertically integrated from 900-200 hPa and later horizontally averaged inside the box. The latter are confined to the surface and therefore only horizontally averaged inside the box.

In Fig. 4.4 and 4.5, we present how the sea level pressure (SLP) and the horizontal winds at 850 hPa respond to the strongest events of LH and SSHF respectively. Starting with the LH-case (Fig. 4.4), a drop in SLP is detected between -12h and +12h inside the box. The drop in SLP indicates ECs to move

through the box. Compared to the wind at -24h and 0h, the winds at -12h are clearly more meridional towards the box and thus indicates the ECs to transport vast amount of warm and humid air into the Gulf Stream region. The strongest LH (0h) is likely because of the strong poleward transport of warm air towards the box prior to the strong LH. We therefore argue that the strong LH connects well with the warm sector of the ECs inside the box.

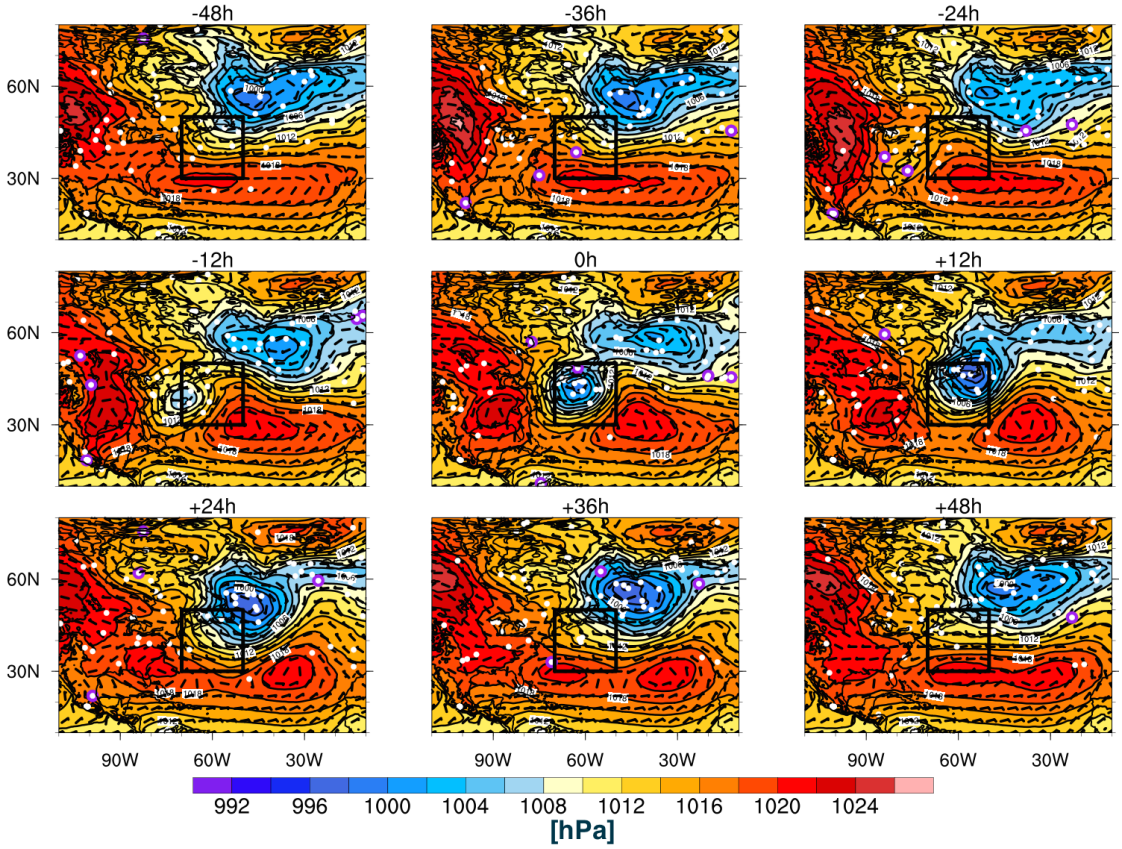

Figure 4.4: Sea level pressure (hPa) and horizontal winds (m/s) at 850 hPa composited for the 90^{th} percentile vertically integrated (900-200 hPa) LH inside the box. At 0h, SLP and winds are composited at the exact time of the 90^{th} percentile LH. Two days positive (+) and negative (-) lag with an interval of 12 hours is also included. Blue (Red) shadings show lower (higher) pressure. White dots with purple ring indicate cyclogenesis, while pure white dots are cyclones originated from an earlier time step.

The decrease in SLP (darker blue shadings) from 0h to +12h in Fig. 4.4 indicates intensifying ECs in the time step after the maximum LH-release. ECs have been shown to intensify due to their own LH-release (e.g., Ludwig et al., 2014), and we hypothesized in section 1.9 that LH-release increases the slope. An increased slope is analogous with an increased baroclinicity, which the ECs can use to grow. The lower SLP at +12h may therefore be an indication of our hypothesis.

To check if there is storm intensification after the strongest LH, we investigate cyclogenesis (white dots with purple ring) and cyclones (white dots) at the composite time. We see a collection of cyclones inside the box at 0h, which indicates the strong LH to be related to a cyclonic pattern. However, only one cyclogenesis event is observed in the box at 0h. Because of the low number of cyclogenesis at 0h, we can not confirm that the increased storm intensity at +12h is a result of LH-release. The intensified cyclonic pattern at +12h may instead just be an artificial effect due to more geographically confined ECs in the composite at this hour.

For the SSHF-events, we see in Fig. 4.5 a noticeable anticyclonic pattern (high pressure pattern) at the east coast of the US. This is in contrast to what we saw for the LH-case (4.4). The anticyclonic pattern in Fig. 4.5 is observed over the continent already at -48h. It persistently stays over the land and seems to slightly intensify towards 0h. The anticyclones clockwise rotation therefore contributes to an equatorwards wind component towards the box in the hours before the strongest SSHF-events. When getting closer to 0h, a more distinct cyclonic pattern is evident on the eastern edge of the box. We therefore suggest a collaboration between the anticyclonic and the cyclonic pattern to generate the strongest SSHF at 0h. The wide spread in blue shadings at -48h and -36h in Fig 4.5 implies that the ECs are weaker and more geographically displaced prior to the peak of the SSHF. It seems like the anticyclones are most important for bringing cold air into the box in the earliest time steps, while the ECs start to play a role closer to the peak of the SSHF. The temporal evolution of the anticyclonic pattern in Fig. 4.5, shows that the anticyclonic pattern intensify before the strongest SSHF (0h) and weakens after the events. Towards 0h, we see an intensification in the cyclonic pattern on

the eastern side of the box.

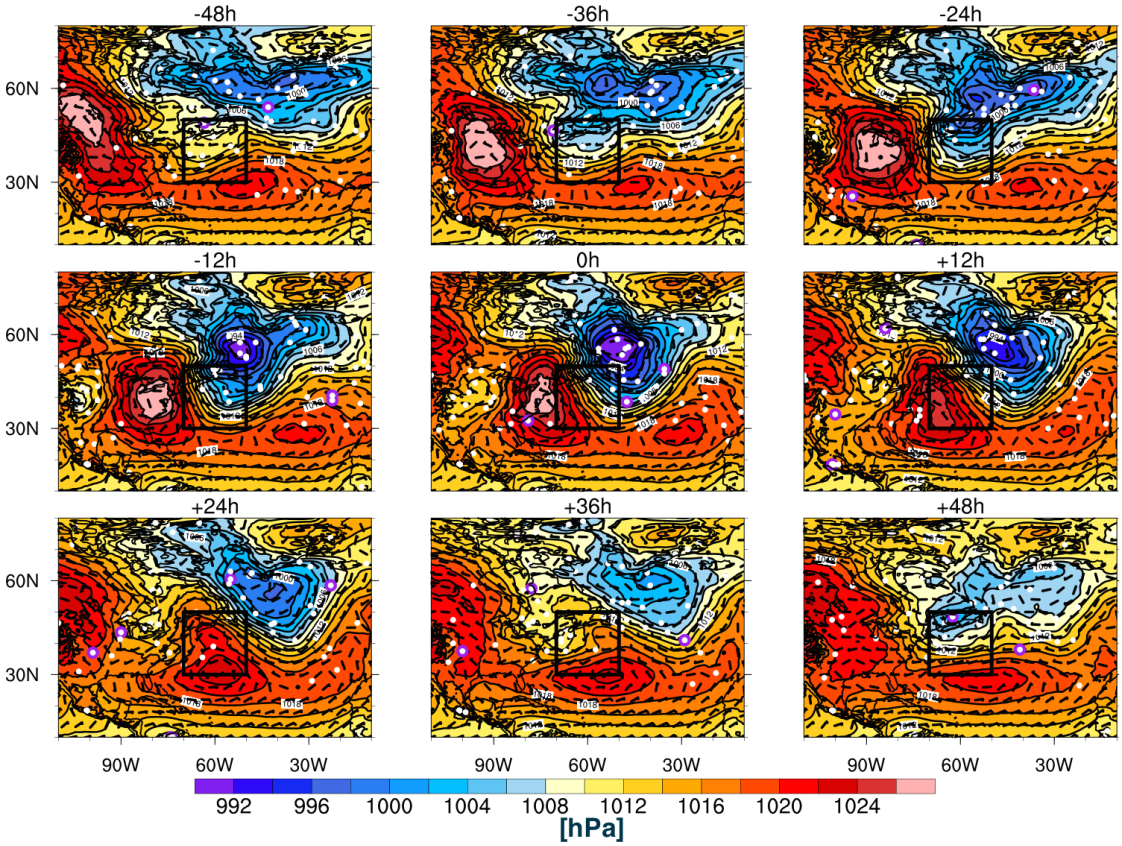

Figure 4.5: Sea level pressure (hPa) and horizontal winds (m/s) at 850 hPa composited for the 90^{th} percentile SSHF inside the box. Shadings and dots show the same as in Fig. 4.4.

Comparable to our findings (4.5), Walsh et al. (2001) performed similar composites in the Gulf Stream region, but for an extended time period (1948-99). Walsh et al. (2001) observed an anticyclonic pattern over the US in the hours before CAOs. They explained the anticyclones to play a role for bringing cold air towards the strong SST-gradient in the NA. Walsh et al. (2001) observed the same temporal evolution of the anticyclonic and cyclonic pattern in their composites and argued that the anticyclones cold air advection potentially makes the region conducive for cyclogenesis and thereby intensifies the cyclonic pattern around the peak of the SSHF. Following the idea of Walsh et al. (2001), the intensified cyclonic

pattern at 0h could therefore be a result of the anticyclones cold air advection inside the box, which generates strong SSHF and possibly enhances baroclinicity through an increase of the isentropic slopes. However, cyclogenesis (white dot with purple ring) is not particularly obvious in the hours before the SSHF-events. This may again indicate that the intensified cyclonic pattern at 0h is more related to the ECs being geographically closer together here.

To support the theory that the strongest SSHF-events are not only dominated by the cyclonic pattern, we use the diagnostics of Iwasaki et al. (2014) (method explained in section 3.4.1) to identify the location of the CAM. For the SSHF-case (Fig. 4.6), deep CAM (blue shadings) is evident in the polar regions, and especially over the Hudson Bay. At the time steps before the strongest SSHF, the CAM in the box is rather shallow (red shadings). When we progress in time, we see a slow southwards deepening of the CAM in the box and around -24h, it starts to penetrate the northern edges. From -24h to 0h, the deep CAM has travelled further towards the center of the box, and at the time of the SSHF-events (0h), a substantial deepening of the CAM can be observed inside the box. This explains the strong values of SSHF at 0h. After 0h, more shallow CAM re-establishes in the box, indicative of warmer air.

The movement of the deep CAM into the box is consistent with the position of the anticyclones in Fig. 4.5. The deep CAM seems to propagate from Hudson Bay with a southwards direction, similar to the anticyclones wind component. It therefore seems like the anticyclones are the main reason for the transport of cold air towards the box, at least in the hours before the strongest SSHF-events.

The composited CAM for the LH-events in Fig. 4.7 shows no clear signals of cold air intrusion at 0h. At this hour, the box is dominated by the cyclones warm sector (Fig. 4.4). A deepening of the CAM is discernible for the LH-events after the ECs have passed the box. At this point (+24h, +36h), the cold sector of the ECs has travelled into the box. The deepening of the CAM is more shallow in the LH-case (Fig. 4.7) compared to the SSHF-case (Fig. 4.6). Thus, the strongest SSHF-events have a deeper CAM at 0 hours, than the LH-events have at +24h (when the ECs cold sector has moved into the box). It indicates stronger CAOs

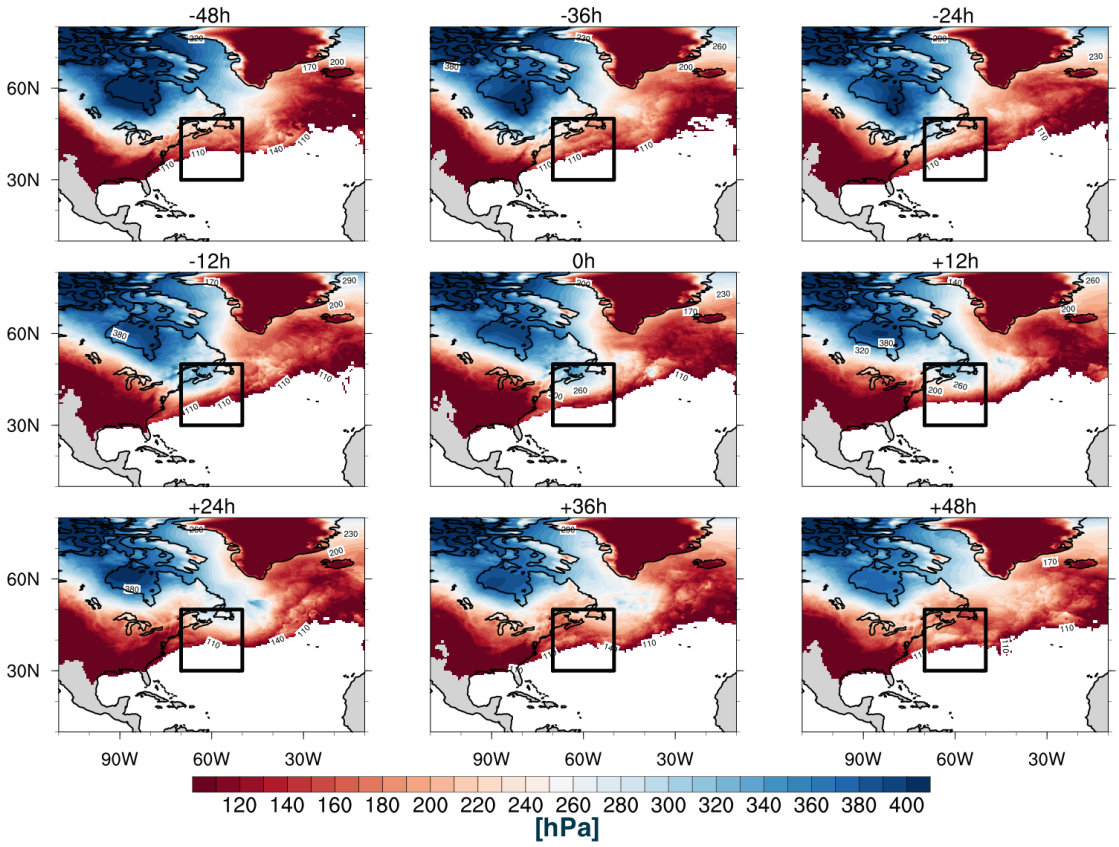

Figure 4.6: Cold Air Mass (hPa) from the difference between $P_s - P_{\theta_{280K}}$ composited for the 90^{th} percentile vertically SSHF inside the box. Blue shadings indicate deeper CAM than red shadings.

for the SSHF-events, which we suggest has to do with the anticyclones in Fig. 4.4.

The distinction between the two cases (SSHF and LH) is also supported by looking at the potential temperature at 850 hPa in Fig. 4.8 and 4.9. For the SSHF-case (Fig. 4.8), we detect a gradually developing cold front, moving towards the box from -12h to +24h. In the LH-case (Fig. 4.9), the cold frontal formation is observed around +24h to +48h. The cold front in the SSHF-case is steeper and we also see colder air inside the box. (blue shadings in Fig. 4.8).

Because the SSHF-events seem to be generated by stronger CAOs in the Gulf Stream region, we suspect the box to be influenced by an upper level trough around the peak of the SSHF. Therefore, as a final comparison, we investigate the

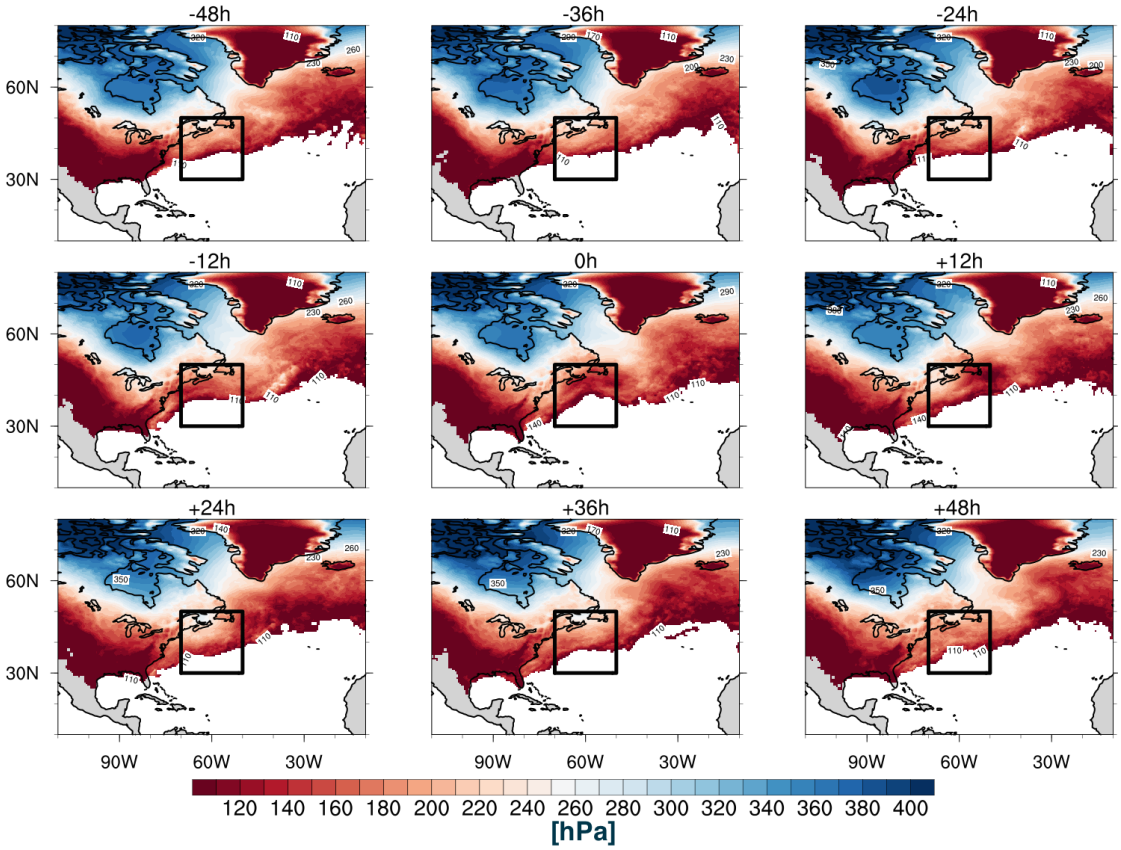

Figure 4.7: Cold Air Mass (hPa) from the difference between $P_s - P_{\theta_{280K}}$ composited for the 90^{th} percentile vertically integrated (900-200 hPa) LH inside the box.

upper troposphere PV for both the SSHF and LH. As explained in section 3.4.2, positive potential vorticity (PV) anomalies are often used to detect such upper level troughs.

We see in Fig. 4.10 and 4.11 that high values of PV are evident at every time steps in the polar regions. This has to do with the cold air sitting there. However, when progressing in time, the SSHF-case (Fig. 4.10) show a substantial amount of PV travelling towards the box around -24h. At 0h, the northern part of the box is penetrated by high values, indicating an upper level trough and cold air advection below the trough. The wind direction in the box is also consistent with the movement of a trough and shows resemblance to a tropopause fold.

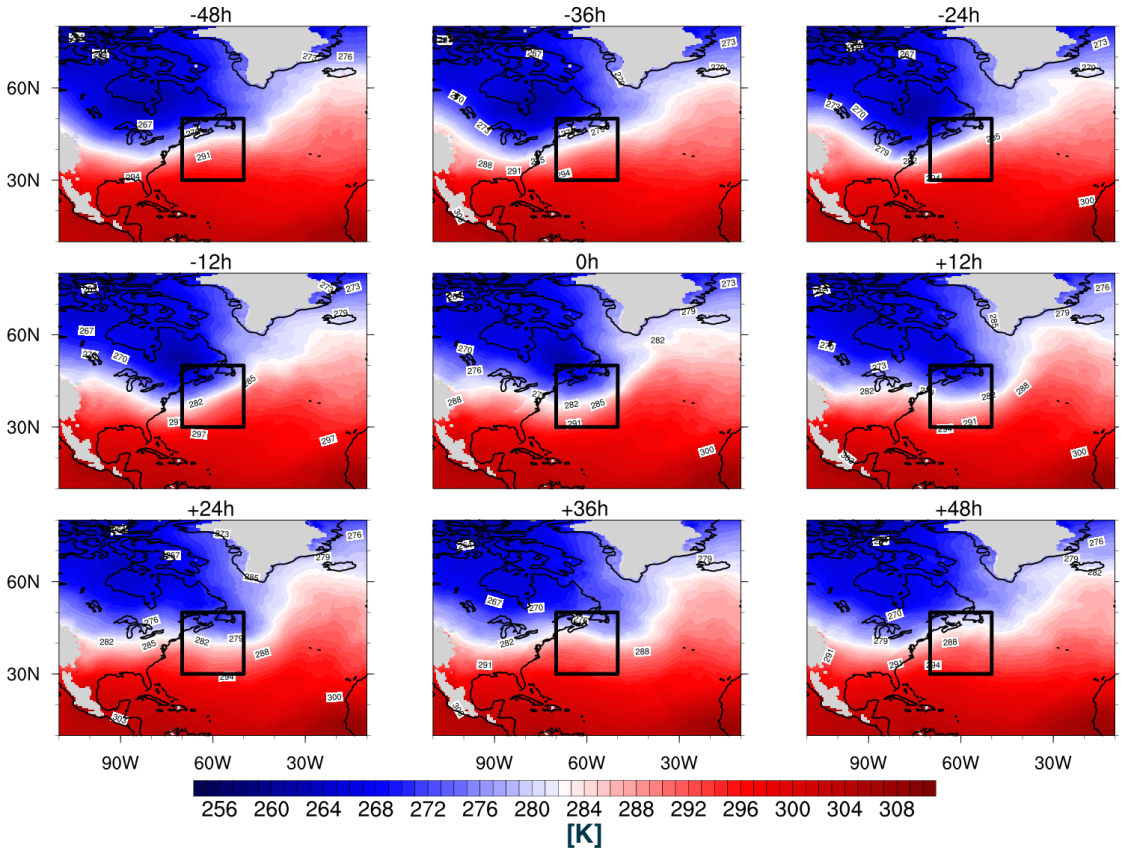

Figure 4.8: Potential temperature (K) at 850 hPa composited for the 90^{th} percentile SSHF inside the box. Blue shadings shows colder θ than red shadings.

Comparing the SSHF-case with the LH-case (Fig. 4.11), weaker values of PV surround the box at the same time as when the ECs warm sector is inside it. When the ECs have transported their cold sector in the box (Fig. 4.4), higher values of PV are discernible (Fig. 4.11), but visibly less than for the SSHF-events (Fig. 4.10). Also, the winds for the LH-events do not have the same distinct change for any of the time steps.

We hypothesized in section 1.9 that when ECs travel along the SST-front, the cold sector of the ECs advect cold air across the SST-gradient. This leads to differential SSHF and may increase the lower level slope. However, our findings show that also anticyclones could generate strong SSHF and thereby also maintain baroclinicity along the SST-front.

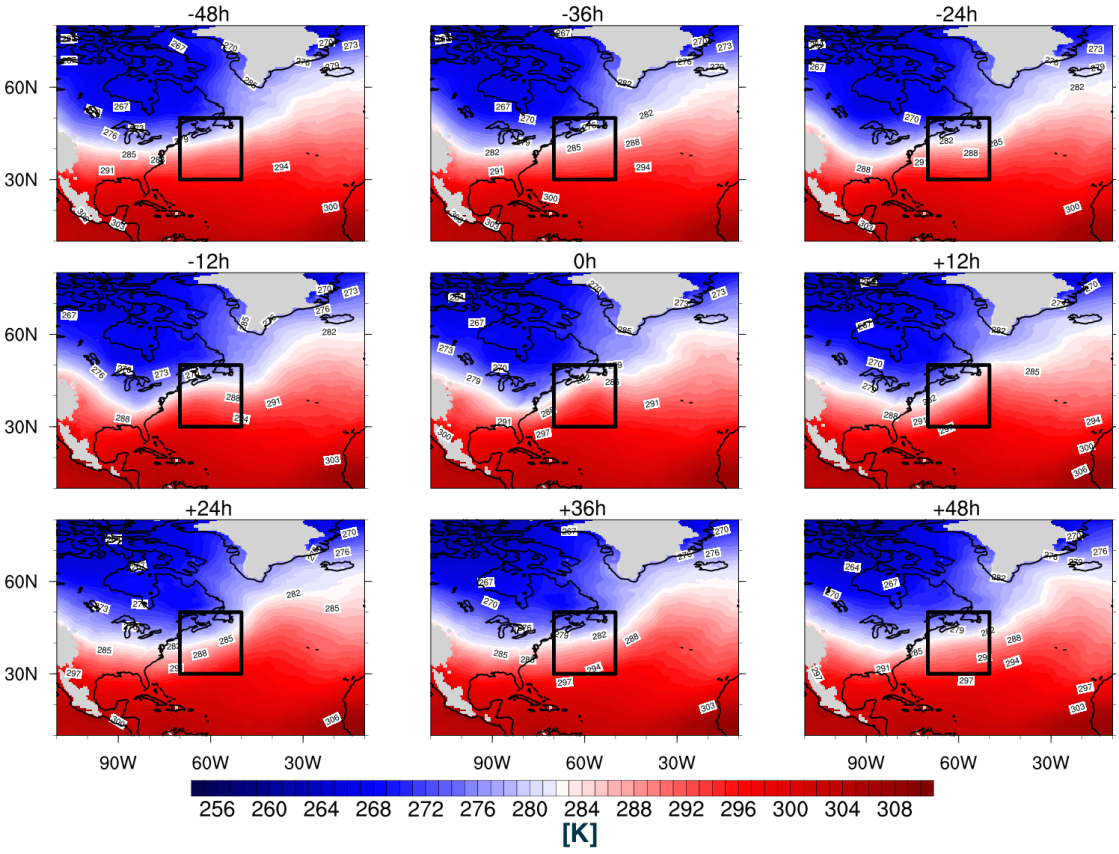

Figure 4.9: Potential temperature (K) at 850 hPa composited for the 90^{th} percentile vertically integrated (900-200 hPa) LH.

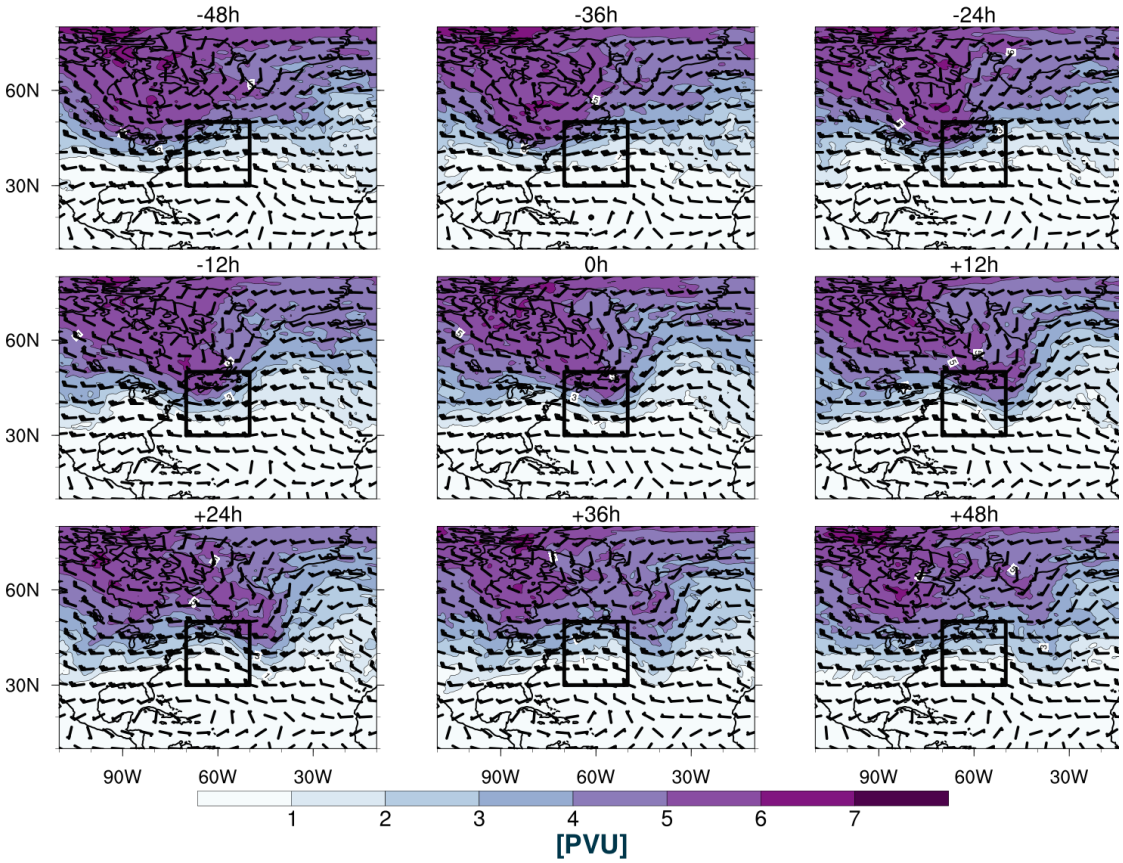

Figure 4.10: Potential Vorticity (PVU) and horizontal wind at 320K composited for the 90^{th} percentile SSHF inside the box. More purple shadings indicate higher PV.

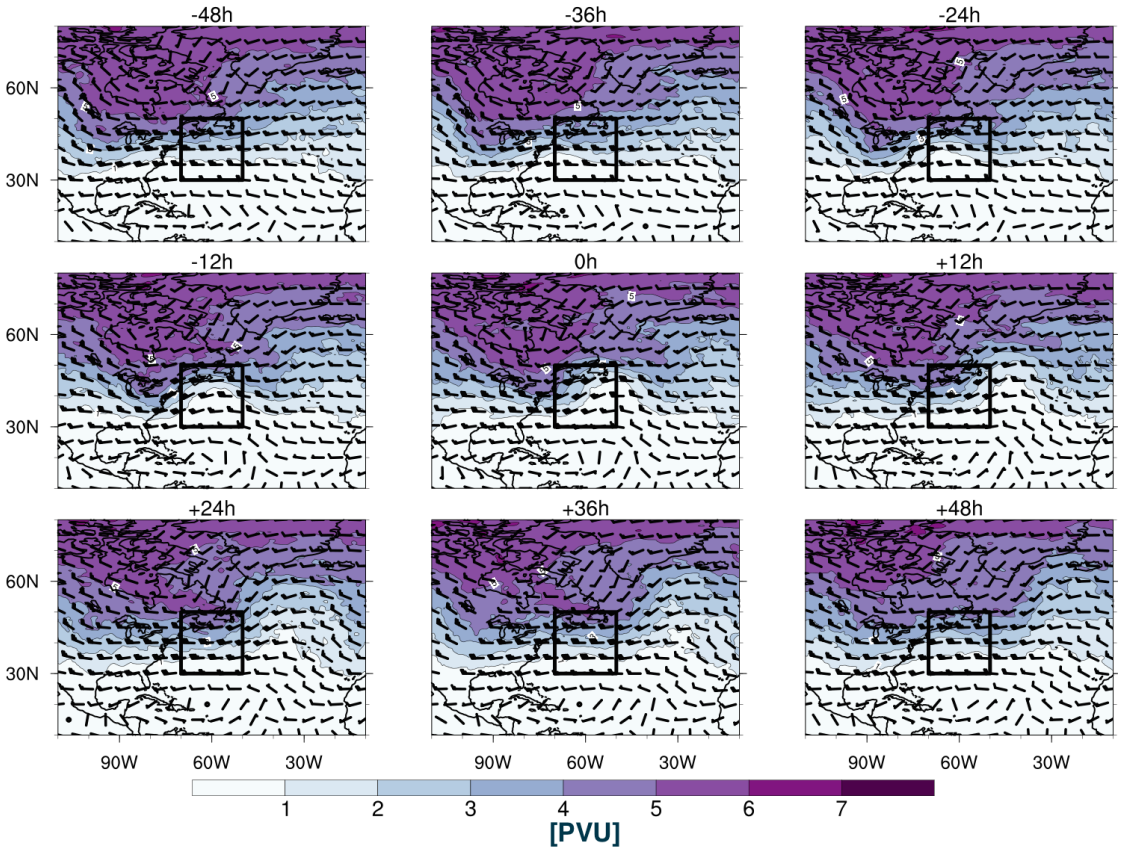

Figure 4.11: Potential Vorticity (PVU) and horizontal wind at 320K composited for the 90^{th} percentile vertically integrated (900-200 hPa) LH inside the box.

4.3 Slope Response to SSHF and LH

4.3.1 All Time Steps

We present a vertical cross correlation analysis between the SSHF and slope in Fig. 4.12a. The SSHF are fixed, meaning that the slope is lagged with respect to the SSHF. We use the same lag-time as the already presented composites (-48h to +48h). Thus, on the right hand side of 0h, the slope is positively lagged with respect to the SSHF. To check the slope response to SSHF in the vertical, we have utilized all available pressure levels up to 200 hPa.

Two distinct regimes are observed in Fig. 4.12a. In the lowest levels, sharp red shadings (strongest positive correlation) are displaced on the right hand side of 0h (positively lagged) and spread out to +24h. The positive correlation on the positively lagged side weakens at later time steps. The strongest positive correlation on the positively lagged side seems to stretch up to 900 hPa. From here and up to around 500 hPa, the strongest positive correlation is shifted to the negatively lagged side.

The two different regimes can be explained by understanding the magnitude of the SSHF at the different vertical levels. If we look back to the vertical cross sections (Fig. 4.2b), we showed large time (DJF) and zonally averaged air-sea temperature differences inside the box. We therefore also assume the box to be a region with strong SSHF. The stronger SSHF we have, the greater magnitude they have on modifying the slope. Close to the surface, the SSHF are strongest, and thus capable of modifying the slope with the highest magnitude. This effect is seen by the positive correlation coefficient on the positively lagged side in Fig. 4.12a. For instance, below 900 hPa, it indicates that an increase (decrease) in SSHF would be followed by an increase (decrease) in the isentropic slope.

When explaining the positive correlation coefficient in the negatively lagged regime, it is again important to understand the magnitude of the SSHF at the different vertical levels. The positive correlation above 900 hPa indicates that an increase (decrease) of slope is followed by an increase (decrease) of SSHF. For instance, an increased slope is expected along frontal zones (Papritz and Spengler,

2015), when cold air is advected into the box. Cold air intrusion in the box thus generates steeper slopes, enhanced air-sea temperature differences and produces strong SSHF. The strong SSHF starts to modify the slope, but because they are mainly confined to the lower troposphere, the SSHF cannot modify the slope at higher levels. This explains the higher up positive correlation coefficient on the negatively lagged side. In the lowest levels however, the SSHF are strong enough to overrule the increased slope in the hours before, which is why we here see a positive correlation coefficient on the positively lagged side.

A disadvantage with the data is that it do not represent the isentropic slope perfectly in regions where the atmosphere is unstable. And during winter, in the lowest part of the troposphere, the Gulf Stream region is often unstable (Stull, 2001). Some cautions should be taken for the positively lagged correlation below 900 hPa, while the data do not have any particular limitations above.

Turning to Fig. 4.12b, we present the same vertical cross correlation as in Fig. 4.12a, but for the correlation between LH and the isentropic slope. The LH is fixed, such that also here the isentropic slope is lagged. In general, the positive correlation (red shadings) is most discernible on the positively lagged side and indicates that an increase (decrease) in LH would be followed by an increase (decrease) in slope. The most confined positive correlation seems to be between 900-500 hPa, consistent with where the LH was found in the vertical cross section in Fig. 4.3a.

Compared with the correlation for the SSHF-case (Fig.4.12a), the maximum positive correlation coefficient is significantly weaker for the LH-case. At the same time as LH works to increase the slope, mechanisms act to reduce the slope as well, for instance the already mentioned tilting of the isentropes (TILT-term in Eq. 1.15). The weak positive correlation is therefore likely a result of different meteorological processes, which all increase and decrease the slope at the same time. And since we, in Fig 4.12b, only look at the slope response from LH, the restoring effects of the slope are all playing a role, but they are hidden. This turns out to be a caveat for the method and makes it difficult to prove that the LH has a significantly increasing effect on the slope.

(a) SSHF and Slope

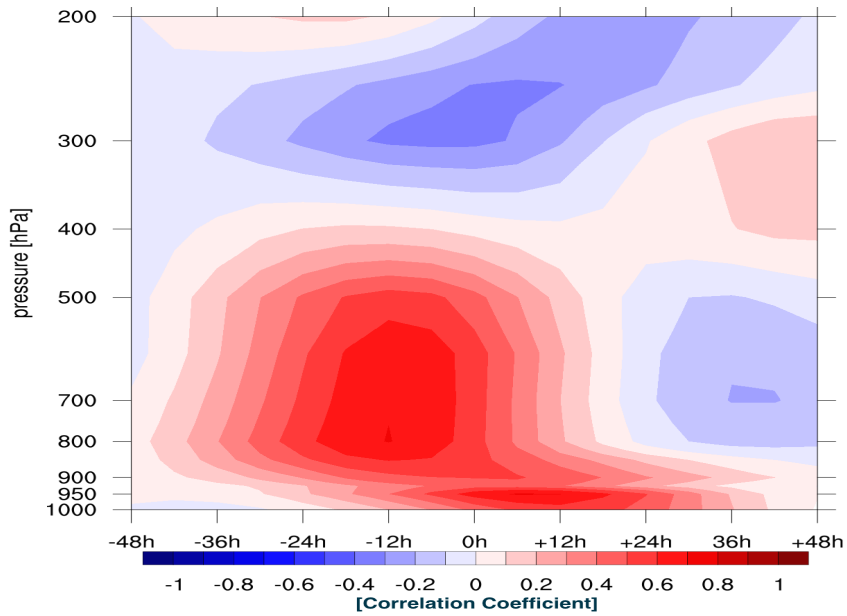

(b) 900-200 hPa LH and Slope

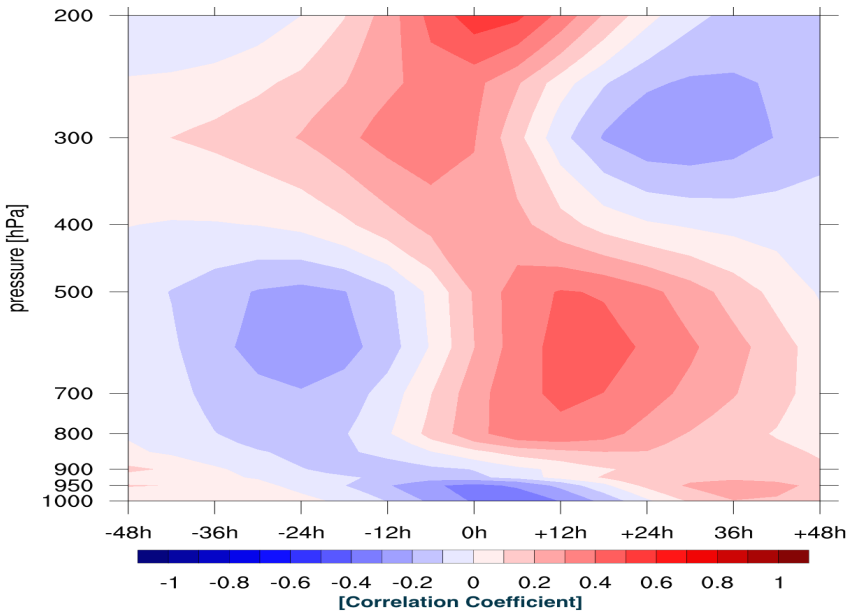

Figure 4.12: Cross correlation at all available pressure levels up to 200 hPa between SSHF and isentropic slope in a) and vertically integrated (900-200 hPa) LH in b). The correlation is taken from the time series inside the black box. Red shadings indicate positive correlation coefficient. If the shadings are positioned on the RHS of 0h, they are positively lagged. The lagged time is two days back and forward in time with a 12h interval.

When looking at the temporal distribution of the positive correlation coefficient in Fig. 4.12b, the maximum correlation at +12h does not necessarily have to do with the LH in the hours before. As shown for the composites, the LH-release is connected to the ECs warm sector inside the box (Fig. 4.4). When the ECs have travelled further through the box, increased slope is generally expected because the cold sector has been transported further east. This change of slope is not directly due to the LH, but a result of a propagating storm. It is likely that the positive correlation seen on the positively lagged side is more related to the position of the ECs, rather than a local slope increase due to LH. That being said, LH-release have been shown to increase the isentropic slope (Papritz and Spengler, 2015), such that there are probably overlapping reasons and not only one unique mechanism causing the weak positive correlation on the positively lagged side. We also showed a positive tendency to increase the slope from LH in the horizontal climatology and the time and zonally averaged vertical cross section of slope tendency from LH (Fig. 4.2b and 4.3b respectively). Hence, the LH probably somehow contributes to the positive correlation on the positively lagged side in Fig. 4.12b, even though the signals are weak.

Also worth to remember that both the slope and the fixed variables (SSHF and LH) are zonally and meridionally averaged for all time steps inside the box. The remaining time series are then correlated with each other, such that all the events are in general highly smoothed. Therefore, a closer analysis of the extreme events is now given.

4.3.2 90^{th} Percentile

This part of the study again investigates the 90^{th} percentile SSHF and LH, but with a greater focus on how they modify the slope. Starting with the former case (Fig. 4.13 and 4.14), the vertical levels are defined by looking at the correlation in Fig. 4.12a. The positively lagged correlation (slope lags SSHF) shifts to the negative side (SSHF lags slope) around 900 hPa. Thus, we present two composited maps of isentropic slope. The first covers the part where the correlation is positively lagged (1000-900) and the second where it shifts to the negative side (900-600).

The vertical integration for the latter stops at 600 hPa, because we mainly focus on the lower tropospheric slope response from SSHF.

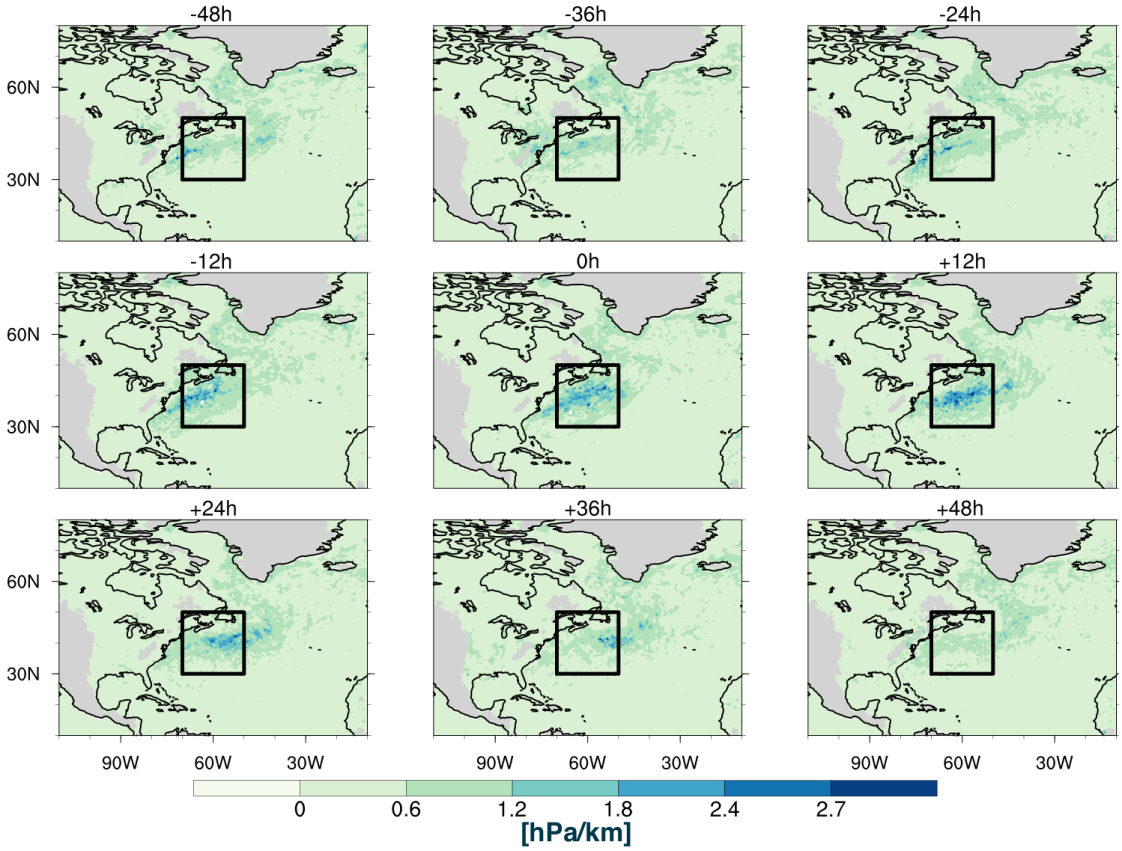

Figure 4.13: Vertically integrated (1000-900 hPa) isentropic slope (hPa/km) composited from the 90^{th} percentile SSHF inside the box. Blue shadings indicate steeper slopes than turquoise shadings.

Let us start to investigate how the lower level slope (1000-900 hPa) responds to the 90^{th} percentile SSHF inside the box (Fig. 4.13). From -48h to 0h, we see a slow increase of slope inside the box. This is consistent with the cold air intrusion seen in Fig. 4.6. Because we have the strongest SSHF at 0h, the SSHF modify the slope at a maximum here. This can explain the increase of slope from 0h to +12h. Though, the enhanced slope is not particularly distinct at +12h, but steeper slopes are detectable.

Consistent with the positive correlation above 900 hPa, the vertically integrated

slope from 900-600 hPa (Fig. 4.14) shows the opposite signals of that in Fig. 4.13. In Fig. 4.14, the strongest slope is discernible 12 hours before the strongest SSHF-events. Since the impact of SSHF on modifying the slope is weak here, the dominating signals are related to the synoptic situation and the intrusion of cold air into the box, which lead to the SSHF-events.

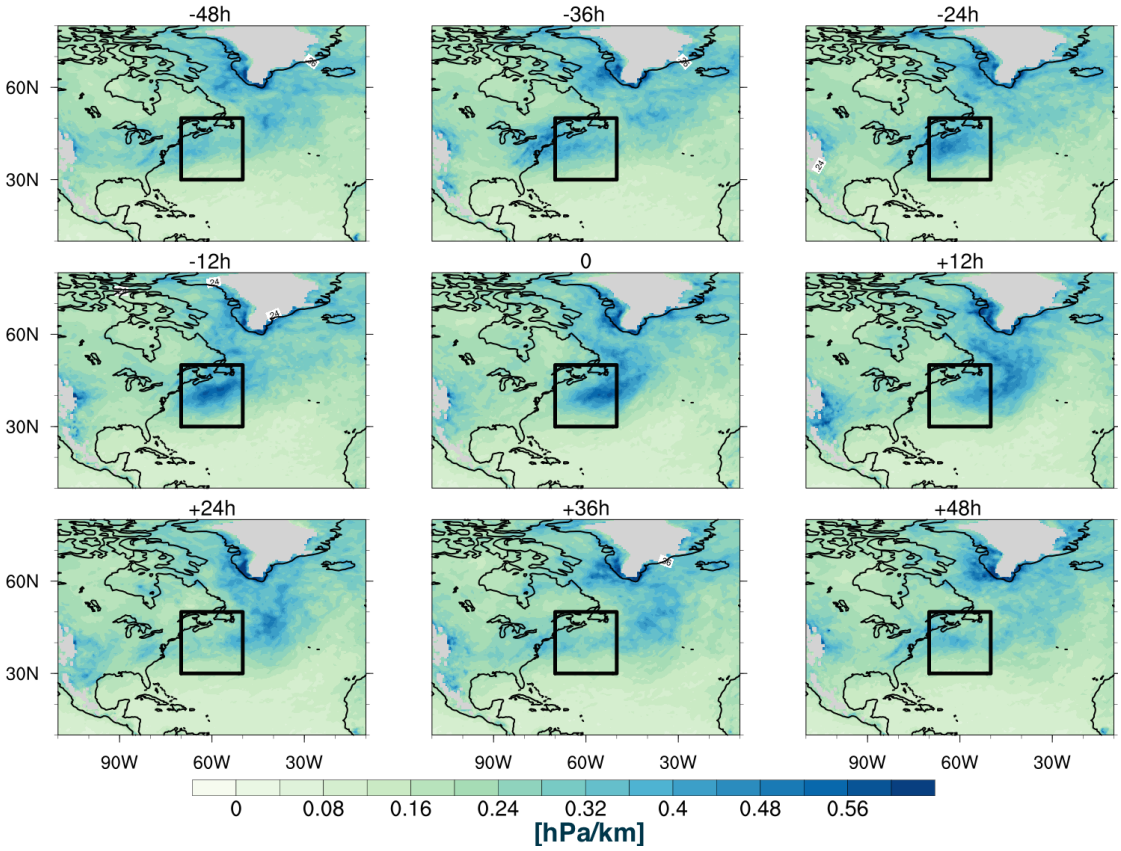

Figure 4.14: Vertically integrated (900-600) isentropic slope (hPa/km) composited from the 90^{th} percentile SSHF inside the box.

The slope response from the 90^{th} percentile SSHF (Fig. 4.13 and 4.14) shows consistency with the vertical cross correlation (Fig. 4.12a). The lower level slope response from SSHF coincides with our initial though that the SSHF act to modify the lower level slope. The fact that the slope response shifts at higher levels is an even stronger indication that the modification of slope from SSHF is confined to the lowest troposphere.

When looking at the LH-case (Fig. 4.15), a first observation is the increase of slope between -24h and -12h. Remembering the synoptic situation, it looked to be at this time step the cyclonic pattern started to form (Fig. 4.4). In the next hours, it evolved in a similar manner to how the slope evolves in Fig. 4.15. At +12h, the strongest slope seems to be more centred inside the box than for the former time steps. It is possible that the LH at 0h maintains or increases the isentropic slope seen in +12h. However, the signals are weak, which leads us to think that the enhanced slope at the time steps after 0h is mainly due to the cold front of the cyclone. With this method, and explained earlier also, it is difficult to quantify the effect LH has on the slope. It is straight forward to look at the LH and the slope individually, but when trying to address how LH alone modifies the slope, it becomes more complicated. For this reason, a closer look on the slope tendency from LH is now given. As the earlier composites, also here the 90^{th} percentile has been used, but instead of having the LH as the composite variable, the slope tendency from LH seems like a better choice. Looking at the slope tendency from LH comes with the advantage that we can quantify the slope tendency purely from LH-release.

At 0h (in Fig. 4.16), we see strong signals of LH at the same time as when the slope tendency from LH is strongest. In the hours both before and after, the LH is significantly weaker. This is not too surprising, considering the fact that we are looking at the slope tendency from LH. That being said, the results are still interesting because it helps us to quantify the effect LH has on the slope in a much higher degree. The positive values for the slope tendency show that there are contributions from LH, which could not be seen for the direct investigation between slope and LH (Fig. 4.12b, 4.15). The positive values in Fig. 4.16 certainly show indications for the LH to increase the slope. This agrees with what we hypothesized in section 1.9.

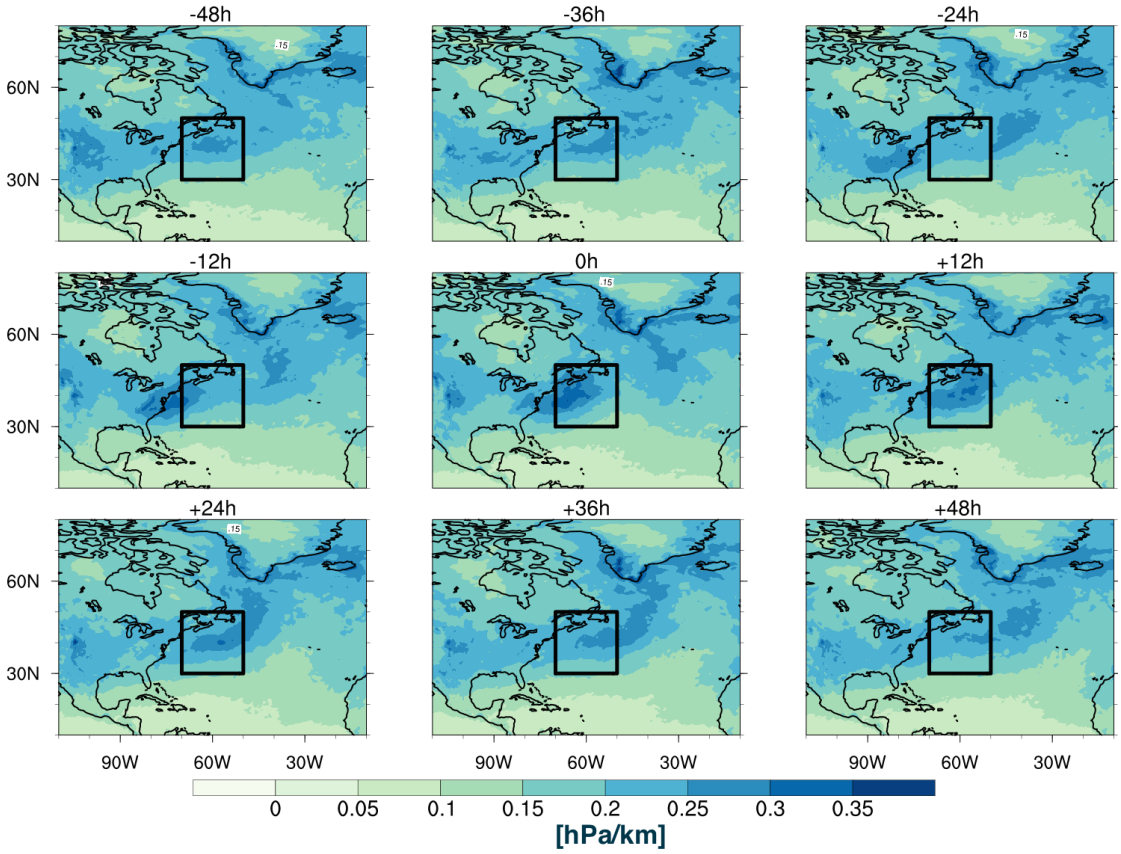

Figure 4.15: Vertically integrated (900-200 hPa) isentropic slope (hPa/km) composited from the 90^{th} percentile vertically integrated (900-200 hPa) LH inside the box.

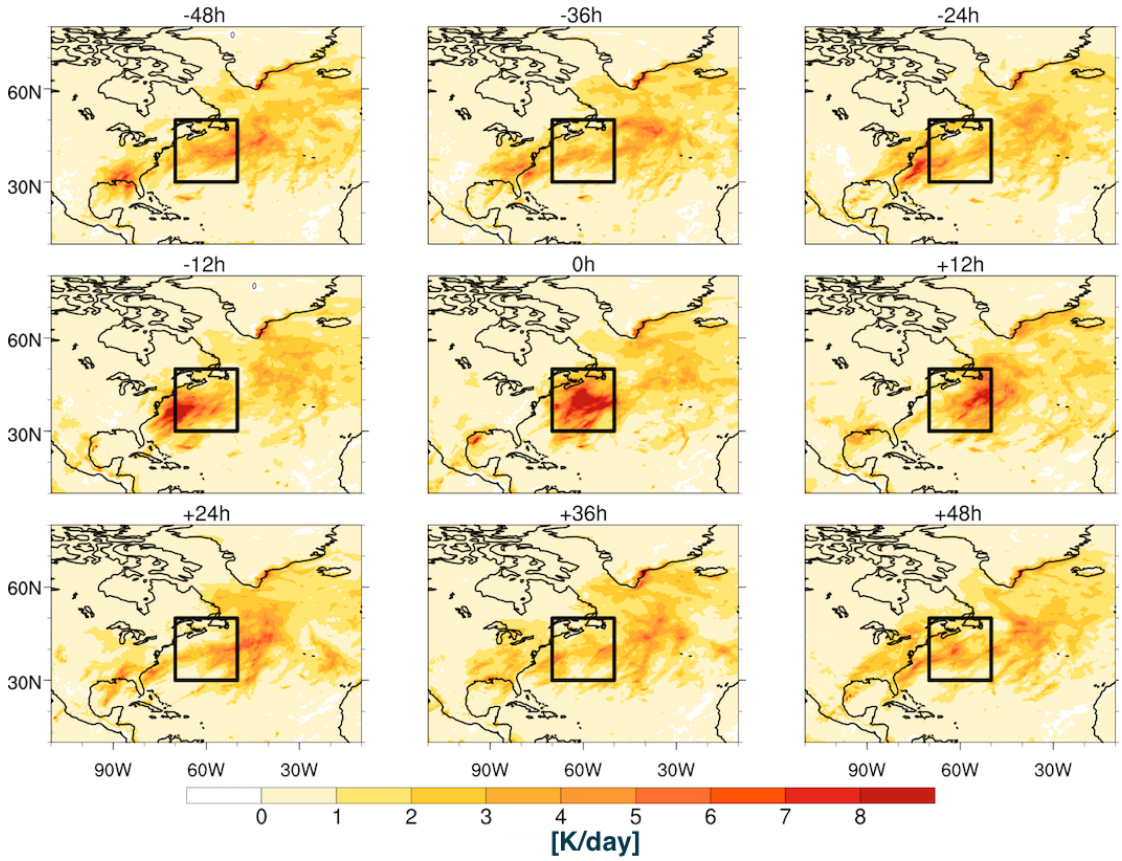

Figure 4.16: Vertically integrated (900-200 hPa) LH (K/day) composited from the 90^{th} percentile vertically integrated (900-200 hPa) slope tendency from LH inside the box. Darkest red shadings indicate strongest LH.

Chapter 5

Concluding remarks

The goal of this study was to advance the understanding of how SSHF and LH maintain baroclinicity in the Gulf Stream region. We used the slope of an isentropic surface as a proxy for baroclinicity and we hypothesized that (i) LH-release over the SST-front increases the slope and maintains baroclinicity in the upper troposphere and (ii) differential SSHF across the SST-front increase the slope and maintain baroclinicity in the lower troposphere.

We focused on a box centred over the strong meridional SST-gradient for DJF 2008-2010 and observed steeper slopes and higher values of LH and SSHF in the box, compared to the rest of the NA.

We explained the 90^{th} percentile LH to be a result of warm air advection from the ECs warm sector and subsequent strong isentropic upglide. For the 90^{th} percentile SSHF, we observed a cyclonic pattern east of the box at the time of the strong SSHF. However, we also revealed a persistent anticyclonic pattern over the North American continent in the hours prior to the peak values of SSHF. We therefore suspected the anticyclones to play an important role in advecting cold air towards the box in the early stages. This was confirmed by observing intrusion of deep CAM in the box, originally from more polar regions and with a path similar to the anticyclones wind component. Our initial thoughts suggested the ECs to be responsible for the strong LH and SSHF inside the box. However, the overall distinctions between the LH- and SSHF-case indicate the latter to not only be

dominated by a cyclonic pattern. We therefore suggest that also anticyclones over the North American continent contribute to the existence of strong SSHF in the Gulf Stream region.

The direct investigation between slope and LH showed a positively lagged positive correlation coefficient above 900 hPa. This indicated an increase in LH to be followed by an increase in slope. That being said, the correlation coefficient was rather weak. We therefore investigated the composited slope for the 90^{th} percentile LH, but did not either find strong signals of increased slope in the hours after LH-release. We argued the moderate signals to likely be related to the mechanisms that restore the slope, i.e. tilting of isentropes through upward and downward vertical wind. We therefore investigated the box integrated 90^{th} percentile slope tendency from LH. It revealed a maxima of LH centred over the box at the same time as the peak values of slope tendency from LH. We could therefore see a contribution from LH to increase the slope. This agrees with (i) of our hypothesis, even though a net increase in slope could not be seen.

For the vertical cross correlation between the isentropic slope and the SSHF, two distinct regimes of positive correlation were observed. The first was a positively lagged regime close to the surface and the second was a higher up negatively lagged regime. The lower (higher) regime indicated an increase in SSHF (slope) to be followed by an increase in slope (SSHF). In addition, the composited slope from the 90^{th} percentile SSHF showed similar signals. Below 900 hPa, we discovered steeper slopes in the hours after strong SSHF. Above 900 hPa, we observed steeper slopes in the hours prior to the peak of SSHF. Hence, the slope response to SSHF in the lowest levels agrees with part (ii) of the hypothesis and the slope response to SSHF at higher levels gives a clear indication that these fluxes are mainly confined to the lowest troposphere.

Our overall findings thus indicate that both SSHF and LH help to maintain baroclinicity in the Gulf Stream region, with the former showing the strongest indications. The SSHF therefore seem to create an environment conducive for strong LH-release when the next ECs enters the box.

5.1 Outlook

For future studies, we suggest to perform similar composites for the 90^{th} percentile LH and SSHF, but for an extended time period. The two winter seasons used in this study are not necessarily representative for the long-term climate in the Gulf Stream. The strong LH and SSHF differ strongly from events to events, where some are more intense than others. The moderate number of events in this study makes it difficult to come with robust conclusions. By extending the time period, more cases can be investigated and potentially give a more complete picture of how the slope responds prior to and after the strongest events. It will also give further insight into the synoptic differences between strong LH- and SSHF-events. Ultimately, such a study may give a better understanding of how LH and SSHF maintain baroclinicity in the Gulf Stream region.

Bibliography

Booth, J. F., Thompson, L., Patoux, J., and Kelly, K. A. (2012). Sensitivity of midlatitude storm intensification to perturbations in the sea surface temperature near the gulf stream. *Monthly Weather Review*, 140(4):1241–1256.

Brayshaw, D. J., Hoskins, B., and Blackburn, M. (2008). The storm-track response to idealized sst perturbations in an aquaplanet gcm. *Journal of the Atmospheric Sciences*, 65(9):2842–2860.

Brayshaw, D. J., Hoskins, B., and Blackburn, M. (2011). The basic ingredients of the north atlantic storm track. part ii: Sea surface temperatures. *Journal of the Atmospheric Sciences*, 68(8):1784–1805.

Businger, S., Graziano, T. M., Kaplan, M. L., and Rozumalski, R. A. (2003). Cold-air cyclogenesis along the gulf-stream front: investigation of diabatic impacts on cyclone development, frontal structure, and track. *Meteorology and Atmospheric Physics*, 000:11–21.

CDO (2016). Climate Data Operators. `http://www.mpimet.mpg.de/cdo`. Last accessed 29.05.16.

Chang, E. K. M., Lee, S., and Swanson, K. L. (2002). Storm track dynamics. *Journal of Climate*, 15:2163–2183.

Chang, E. K. M. and Orlanski, I. (1993). On the dynamics of a storm track. *Journal of the Atmospheric Sciences*, 50:999–1015.

Chou, S.-H. and Ferguson, M. P. (1991). Heat fluxes and roll circulations over the western gulf stream during an intense cold-air outbreak. *Boundary-Layer Meteorology*, 55(3):255–281.

Eady, E. T. (1949). Long waves and cyclone waves. *Tellus*, 1:33–52.

ECMWF (2015). Official IFS Documentation. `https://software.ecmwf.int/wiki/display/IFS/CY41R1+Official+IFS+Documentation`. Last accessed 11.05.16.

Emery, W. J. and Thomson, R. E. (2001). *Data Analysis Methods in Physical Oceanography*. Elsevier.

Hartmann, D. L. (1994). *Global physical climatology*. Academic Press.

Hinman, R. (1888). *Eclectic physical geography*. Sampson Low.

Holton, J. R. and Hakim, G. J. (2012). *An introduction to dynamic meteorology*. Academic press.

Hoskins, B., Pedder, M., and Jones, D. W. (2003). The omega equation and potential vorticity. *Quarterly Journal of the Royal Meteorological Society*, 129:3277–3303.

Hoskins, B. J. and Valdes, P. J. (1990). On the existence of storm-tracks. *Journal of the Atmospheric Sciences*, 47:1854–1864.

Hotta, D. and Nakamura, H. (2011). On the significance of the sensible heat supply from the ocean in the maintenance of the mean baroclinicity along storm tracks. *Journal of Climate*, 24:3377–3401.

Iwasaki, T., Shoji, T., Kanno, Y., Sawada, M., Ujiie, M., and Takaya, K. (2014). Isentropic analysis of polar cold airmass streams in the northern hemispheric winter. *Journal of the Atmospheric Sciences*, 71(6):2230–2243.

Ludwig, P., Pinto, J. G., Reyers, M., and Gray, S. L. (2014). The role of anomalous SST and surface fluxes over the southeastern North Atlantic in the explosive development of windstorm Xynthia. *Quarterly Journal of the Royal Meteorological Society*, 140:1729–1741.

Madonna, E., Wernli, H., Joos, H., and Martius, O. (2014). Warm conveyor belts in the era-interim dataset (1979–2010). part i: Climatology and potential vorticity evolution. *Journal of Climate*, 27:3–26.

Markowski, P. and Richardson, Y. (2010). *Mesoscale Meteorology in Midlatitudes*. John Wiley and Sons, Ltd.

Marshall, J. and Plumb, R. (2007). *Atmosphere, Ocean and Climate Dynamics: An Introductory Text*. International Geophysics. Elsevier Science.

Minobe, S., Kuwano-Yoshida, A., Komori, N., Xie, S.-P., and Small, R. J. (2008). Influence of the Gulf Stream on the troposphere. *Nature*, 452:206–209.

Nakamura, H., Sampe, T., Goto, A., Ohfuchi, W., and Xie, S.-P. (2008). On the importance of midlatitude oceanic frontal zones for the mean state and dominant variability in the tropospheric circulation. *Geophysical Research Letters*, 35:L15709.

Nakamura, H., Sampe, T., Tanimoto, Y., and Shimpo, A. (2004). Observed associations among storm tracks, jet streams and midlatitude oceanic fronts. *The Earth's Climate: The Ocean-Atmosphere Interaction*, 147:329–346.

Palmer, T. N. and Zhaobo, S. (1985). A modelling and observational study of the relationship between sea surface temperature in the north-west atlantic and the atmospheric general circulation. *Quarterly Journal of the Royal Meteorological Society*, 111(470):947–975.

Papritz, L., Pfahl, S., Sodemann, H., and Wernli, H. (2014). A climatology of cold air outbreaks and their impact on air-sea heat fluxes in the high-latitude South Pacific. *Journal of Climate*, 28:342–364.

Papritz, L. and Spengler, T. (2015). Analysis of the slope of isentropic surfaces and its tendencies over the north atlantic. *Quarterly Journal of the Royal Meteorological Society*, 141(693):3226–3238.

Pfahl, S., Madonna, E., Boettcher, M., Joos, H., and Wernli, H. (2014). Warm conveyor belts in the ERA-Interim dataset (1979-2010). Part II: Moisture origin and relevance for precipitation. *Journal of Climate*, 27:27–40.

Pidwirny, M. (2006). The fundamentals of physical geography (2nd edition). `http://www.physicalgeography.net/fundamentals/contents.html`. Last accessed: 20.05.16.

Rasmussen, E. and Turner, J. (2003). *Polar Lows: Mesoscale Weather Systems in the Polar Regions*. Cambridge University Press.

Sampe, T., Nakamura, H., Goto, A., and Ohfuchi, W. (2010). Significance of a midlatitude SST frontal zone in the formation of a storm track and an eddy-driven westerly jet. *Journal of Climate*, 23:1793–1814.

Shaman, J., Samelson, R. M., and Skyllingstad, E. (2010). Air–sea fluxes over the gulf stream region: Atmospheric controls and trends. *Journal of Climate*, 23(10):2651–2670.

Small, R., Tomas, R. A., and Bryan, F. O. (2014). Storm track response to ocean fronts in a global high-resolution climate model. *Climate Dynamics*, 43:805–828.

Stull, R. B. (2001). *An introduction to boundary layer meteorology*. Kluwer Academic Publisher, Dordrecht.

Talley, L. D., Pickard, G. L., Emery, W. J., and Swift, J. (2011). *Descriptive Physical Oceanography, An Introduction*. Elsevier, Oxford, U.K.

The National Center for Atmospheric Research (2016). . `http://www2.cgd.ucar.edu/research/interdisciplinary-projects/yotc/about`. Last Accessed 23.04.16.

The NCAR Command Language (2015). Version 6.3.0. `http://www.ncl.ucar.edu`. Last Accessed 29.05.16.

Vannière, B., Czaja, A., Dacre, H., Woollings, T., and Parfitt, R. (2016). A potential vorticity signature for the cold sector of winter extratropical cyclones. *Quarterly Journal of the Royal Meteorological Society*, 142:432–442.

Vavrus, S., Walsh, J. E., Chapman, W. L., and Portis, D. (2006). The behavior of extreme cold air outbreaks under greenhouse warming. *International Journal of Climatology*, 26(9):1133–1147.

Wallace, J. M. and Hobbs, P. V. (2006). *Atmospheric Science An Introductory Survey*. Elsevier.

Walsh, J. E., Phillips, A. S., Portis, D. H., and Chapman, W. L. (2001). Extreme cold outbreaks in the united states and europe, 1948–99. *Journal of Climate*, 14(12):2642–2658.

Warner, T. (2011). *Numerical Weather and Climate Prediction*. Cambridge University Press.

Woollings, T., Hoskins, B., and M.Blackburn (2010). Storm track sensitivity to sea surface temperature resolution in a regional atmosphere model. *Climate Dynamics*, 35:341–353.

World Meteorological Organization (2008). The YOTC Science plan. `https://www.wmo.int/pages/prog/arep/wwrp/new/documents/YOTC_Science_Plan.pdf`. Last Accessed 23.04.16.

Xue, H. and Bane, J. M. (1997). A numerical investigation of the gulf stream and its meanders in response to cold air outbreaks. *Journal of Physical Oceanography*, 27(12):2606–2629.